



Seismic Fragility of Code-conforming Italian Buildings Based on SDoF Approximation

Akiko Suzuki  and Iunio Iervolino 

Dipartimento di Strutture per l'Ingegneria e l'Architettura, Università degli Studi di Napoli Federico II, Naples, Italy

ABSTRACT

The paper presents and discusses seismic fragility functions of code-conforming buildings in Italy. The structures under consideration are taken from those considered by a large Italian research project (RINTC), aiming at evaluating the seismic reliability of new-design buildings. Design refers to a variety of structural typologies (i.e. un-reinforced masonry, reinforced concrete, steel, and precast concrete buildings) and configurations (e.g. number of stories, floor plan, and the presence of infills), as well as to sites with different hazard levels and local site conditions. The seismic fragility of the structures is evaluated via multiple-stripe nonlinear dynamic analysis using the equivalent-single-degree-of-freedom (ESDoF) systems calibrated based on pushover analysis of the three-dimensional structural models. The seismic response of the ESDoF models is also validated in terms of demand-capacity ratio and risk of failure compared to those of the three-dimensional structural models. Along with providing fragility curves for the buildings located at high-hazard sites, the study discusses the issues that significantly affect the fragility assessment for those located at low-to-mid hazard sites.

ARTICLE HISTORY

Received 30 November 2018
Accepted 11 August 2019

KEYWORDS

Performance-based earthquake engineering; seismic risk; vulnerability; nonlinear dynamic analysis; collapse risk

1. Introduction

In the current Italian building code (NTC hereafter) (CS.LL.PP., 2008, 2018), somewhat similar to Eurocode 8 (EC8) (CEN 2004), structural performance has to be verified with respect to seismic actions (i.e. ground motion, GM, intensity) with specific *return periods* (T_R) of exceedance at a site of interest. In case of ordinary structures, for example, safety verifications for *damage limitation* and *life-safety* limit states are required against GM intensity measure (IM) levels corresponding to T_R of 50 and 475 years, respectively. However, seismic structural reliability resulting from design is not explicitly controlled although design seismic actions have a probabilistic determination.

To quantitatively address the seismic risk that the code-conforming design exposes structures to, a large research project was carried out in Italy over the past few years. In the project, named *Rischio Implicito – Norme Tecniche per le Costruzioni* (RINTC; see acknowledgements), structures belonging to a variety of structural types (i.e. un-reinforced masonry; URM, reinforced-concrete; RC, precast-reinforced concrete; PRC, steel; S, and base-isolated reinforced-concrete buildings) and configurations were designed according

CONTACT Akiko Suzuki  akiko.suzuki@unina.it  Dipartimento di Strutture per l'Ingegneria e l'Architettura, Università degli Studi di Napoli Federico II, via Claudio 21, Naples 80125, Italy

Color versions of one or more of the figures in the article can be found online at www.tandfonline.com/ueq.

to NTC for a number of sites featuring different hazard levels (Milan, Caltanissetta, Rome, Naples, and L'Aquila) and local site conditions (A and C according to EC8 classification). For all the buildings under consideration, seismic structural reliability was assessed in terms of mean annual failure rate with respect to *global collapse* and *usability-preventing damage* within the performance-based earthquake engineering (PBEE) framework (Cornell and Krawinkler 2000). For each building the failure probability was computed at discrete IM levels via nonlinear dynamic analysis using three-dimensional (3D) structural numerical models, and then integrated with the seismic hazard for the building site (Iervolino, Spillatura, and Bazzurro 2018; RINTC-Workgroup 2018).

Since fragility curves were neither needed nor obtained in the RINTC project, this study aims at developing hazard-consistent seismic fragility curves for code-conforming building structures in the Italian context, referring to the prototype buildings examined in the mentioned project. There is a variety of procedures to derive fragility functions such as post-earthquake damage observations, numerical structural analysis, or expert judgment. Analytical approaches, in particular, have been developed in the last decades to help when viable data from real earthquake damage are unavailable or insufficient (Jalayer et al. 2017; Ptilakis, Crowley, and Kaynia 2014; Silva et al. 2019). They can be broadly classified into two subclasses depending on whether they are based on nonlinear static or dynamic analyses. The former approach involves the characterization of a static capacity curve (i.e. a force–displacement relationship for the structure) via nonlinear static analysis and its comparison with a demand curve; i.e. Capacity Spectrum Method or so-called HAZUS methodology (HAZUS-MH 2003). The latter characterizes the ground motion versus seismic demand relationship via time-history response analysis using GM recordings, which allows to directly account for *record-to-record variability* of structural response; e.g. Rota, Penna, and Magenes (2010). A hybrid approach is also often applied, that is characterizing the static capacity curve via pushover analysis, then carrying out dynamic analysis with an equivalent single-degree-of-freedom (ESDoF) system (D'ayala, Vamvatsikos, and Porter 2014; Kosič, Fajfar, and Dolšek 2014). This combination has the advantage, especially when examining a large number of structures, of including the uncertainty of structural dynamic response with manageable computational demand.

Herein, the fragility functions are computed via nonlinear dynamic analysis of ESDoF systems. In particular, *multiple-stripe analysis* (MSA) (Jalayer and Cornell 2003), is carried out using *hazard-consistent* GM record sets as well as using a GM set collected from large seismic events for comparison purposes (i.e. to investigate the issues which arise with fragility derivation for the structures designed for the low-to-mid seismicity sites). The ESDoF models are first validated through the comparison with the 3D structural models, in terms of nonlinear structural response for all considered cases. Subsequently, the collapse fragility functions, expressed in terms of spectral acceleration at a period close to the fundamental vibration periods of the corresponding structure (to follow), are fitted via a maximum likelihood criterion. The study primarily provides seismic fragility of the buildings designed for the high-hazard sites for which the fragility functions can be compared with those obtained using the 3D models then discusses those for the low-to-mid hazard sites addressing issues related to GM selection that affect the resulting fragility significantly. For all considered cases, the annual failure rates derived from the obtained seismic fragility curves are also compared with those of the original 3D models. The results of this study could contribute to the next generation of performance-based seismic design towards the implementation of an explicit probabilistic seismic risk assessment in modern building codes (ASCE 2017).

The remainder of the paper is structured such that the next section describes the characteristics of the prototype buildings covered in the study, including their ESDoF characterization. Subsequently, the methodology for fitting fragility functions of the buildings designed for the high-hazard sites is presented, followed by the discussion on the estimated fragility parameters and the comparison of the annual failure rates with the original 3D models for each structural type. Furthermore, the issues related to the low-to-mid hazard sites are described highlighting the sensitivity of the resulting fragility on the GM record selection. A summary with final remarks closes the study.

2. Seismic Design Features and Structural Models

Among the buildings designed in the RINTC project, this study exclusively examines some regular buildings belonging to four different structural types (i.e. URM, RC, S, and PRC buildings) and located at three sites (i.e. Milan, Naples, and L'Aquila, hereafter denoted as MI, NA, AQ, respectively) representing low-, mid- and high-hazard in Italy. In the project, the 3D numerical models for structural analysis were constructed in OpenSees (McKenna et al. 2000) except for URM buildings that were analyzed using TREMURI (Lagomarsino et al. 2013); see (Cattari et al. 2018; Magliulo et al. 2018; Ricci et al. 2018; Scozzese et al. 2018) for typology-specific modelling. In the following, the main features of the considered buildings are first reviewed, followed by the methodology and derivation of the ESDoF models.

2.1. Life-safety and Damage Limitation Design Seismic Actions

NTC mentions that structural systems must withstand the design seismic action with the return period of exceedance corresponding to the limit state of interest at the building site. For ordinary structures, which were examined in the RINTC project, design seismic actions are prescribed by means of elastic response spectra for the *damage limitation* (SLD) and *life-safety* (SLV) limit states, $Sa_{SLD}(T)$ and $Sa_{SLV}(T)$, which are close approximations of the 50- and 475-year return period uniform hazard spectra (UHS) at the building site, respectively. Figure 1 shows the official Italian seismic hazard map in terms of peak ground acceleration (PGA) with 475-year return period of exceedance on rock and the code-prescribed horizontal elastic response spectra for the considered three sites (under two soil conditions A and C according to EC8 classification (CEN 2004)).

In case that linear analysis is carried out for design, the code allows to introduce a behavior factor, q , to reduce the elastic strength demand indirectly accounting for plastic excursion beyond the elastic limit (i.e. ductility and energy dissipation capacity). Thus, design seismic action is obtained from the elastic response spectra divided by the q factor prescribed depending on structural typology, configuration, regularity, and ductility class.

2.2. Prototype Buildings of the RINTC Project

2.2.1. Residential URM Buildings

A series of two- or three-story (2st, 3st) URM buildings made of perforated clay units with mortar joints was designed with a variety of different architectural configurations for the three sites on both the soil conditions A and C. Specifically, eight different (in plan) architectural configurations, either regular or irregular according to the definition

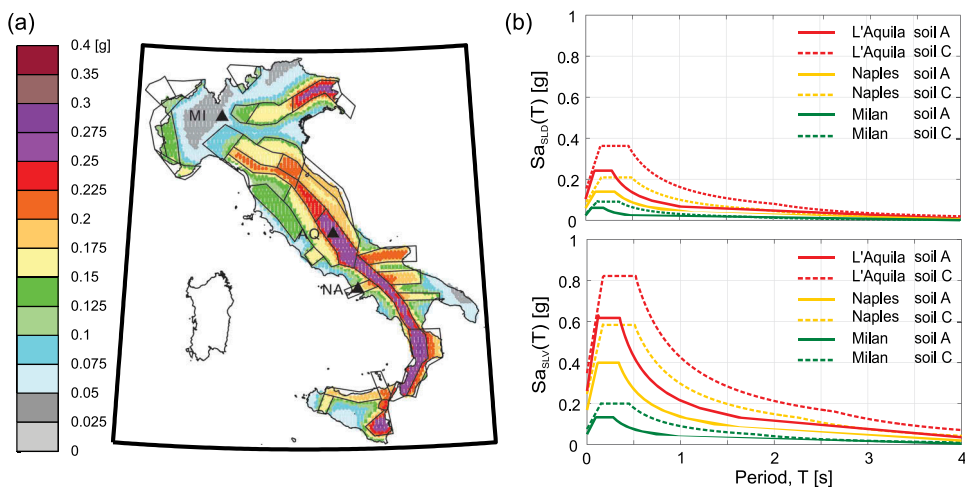


Figure 1 Seismic hazard at the three sites under consideration; (a) official Italian seismic source zones and hazard map in terms of PGA with 475-year return period of exceedance on rock; (b) design elastic spectra corresponding to 50-year (top) and 475-year return periods (bottom).

provided by NTC, were considered so as to represent typical Italian residential buildings: regular C (C1-C7 to be defined later), E2, E8, E9 and irregular I, E5, F, and G types (Cattari et al. 2018; Manzini et al. 2018). For the purpose of investigation, the buildings with the different configuration types were first designed, given some structural features in common (e.g. materials and typologies of horizontal diaphragms). Then, the building-site combinations that had yielded a code-conforming, yet not over-dimensioned, building design were selected based on a *global safety factor*, which was defined as the ratio of PGA level causing the attainment of the ultimate structural capacity to the 475-year return period design level (Manzini et al. 2018). The applied design methods are: *simple building* (SB) rules, *linear static analysis* (with equivalent frame, LSA-F, or with cantilever modeling, LSA-C), and *nonlinear static analysis* (NLSA).¹ In case of LSA, design seismic action was determined by the elastic response spectra divided by a behavior factor q of 3.6. Among the configurations designed in the project, this study exclusively examined those with regularity both in plan and in elevation (i.e. C and E2, E8, E9), which amount to 31 building-site combinations in total. For further details on the structural design of the examined regular buildings, as well as the other irregular building cases, see Manzini et al. (2018) and Cattari et al. (2018).

C-type configuration: Fig 2a,b show the 3D model and the plan of a C-type configuration building, which is regular in both plan and elevation. For this type of configuration, two- and three-story 5×2 bays masonry buildings with a variety of wall thickness (i.e. percentage of resistant area, A_{res}) were designed. The floor area of each building is $22.5 \times 12.3 \text{ m}^2$, and each story height is 3.1 m. For each number of stories, seven configurations with different thickness of the load-bearing walls, denoted as C1-C7, were designed as to cover the possible minimum A_{res} prescribed by the design code: C1 with the smallest A_{res} of the floor, 4.4%; C7 with the largest, $\geq 7\%$; C2-C6 with the intermediate values. Among the considered C-type buildings, 16 building-site combinations in total (as it will be clarified later) were considered to have met the design criteria for the three sites.

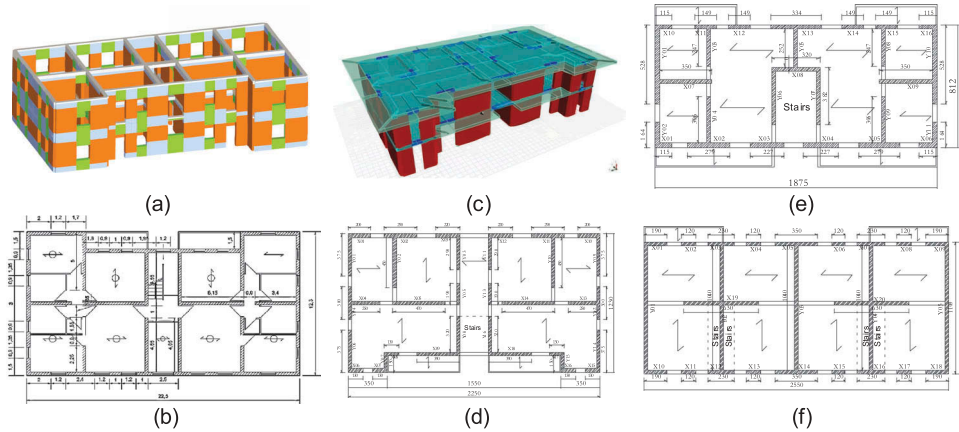


Figure 2 Examples of the prototype URM buildings; (a) 3D view of the two-story C-type building (with equivalent frame model); (b) C-type plan; (c) 3D view of the two-story E2-type building (with equivalent frame model); (d) E2-type plan; (e) E8-type plan; (f) E9-type plan.

E-type configurations (E2, E8, E9): the panels c-f of Fig. 2 show the 3D model of the E2 building and the plans of the three different configurations, E2, E8, and E9, respectively, all of which are regular in both plan and elevation. The floor area ranges between approximately $150 \text{ m}^2 - 290 \text{ m}^2$, and each plan is characterized by a layout of masonry walls different from one another. As for the C-type configuration, two- and three-story buildings with 3.1 m story were designed, then the design solutions for each site were identified based on the global safety factors. As a result, the 15 building-site combinations in total were examined in this study.

2.2.2. Residential RC Buildings

In the RINTC project, a series of three-, six-, and nine-story (3st, 6st, 9st) RC moment-resisting frame (MRF) buildings and nine-story RC shear wall buildings were designed for each of the three sites with different levels of seismicity (soil C for all sites and soil A only for AQ), including considerations on soil-structure interaction and modelling uncertainty for some selected cases (Franchin et al. 2018; RINTC-Workgroup 2018). In cases of the MRFs, three different structural configurations (i.e. bare-, infilled-, and *pilotis*-frames, hereafter denoted as BF, IF, and PF, respectively; Fig. 3a) were considered, and this study exclusively examined all of those without modeling uncertainty and soil-structure interaction. The buildings were intended for residential use and are all 5×3 bays MRFs characterized by regularity in plan (Fig. 3b) and elevation. The floor area of the buildings is approximately $21.4 \times 11.7 \text{ m}^2$, which is common for all cases. The ground floor height and all other story heights are 3.4 and 3.05 m, respectively. The RC frames include knee-joint beams designed to bear the staircases. From a design point of view, the structural members of BF and IF are identical in dimensions and reinforcement detailing (i.e. the difference lies in the presence of infills) while the vertical structural members at the ground floor of PF were strengthened to account for the infill reduction, as per code requirements.

For each site, seismic design was performed by means of modal response spectrum (MRS) analysis. The reference design strength was assigned by the design response

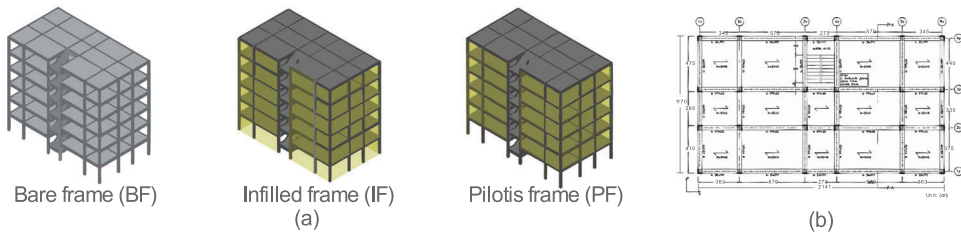


Figure 3 Examples of the prototype RC buildings; (a) six-story BF, IF, PF buildings; (b) plan view.

spectrum obtained from the horizontal elastic response spectrum for soil C (Fig. 1b) divided by a behavior factor $q = 3.9$ (for multi-story RC frames in low ductility class; note that masonry infills are not explicitly accounted for in the NTC code-conforming design, hence the reference to BF alone covering all frames). For more details on the structural design and subsequent numerical modeling, see Ricci et al. (2018).

2.2.3. Industrial Steel Buildings

A series of industrial steel buildings was designed for the three sites on both the soil conditions A and C. As shown in Fig. 4, each building, equipped with an overhead traveling crane, consists of five transverse single-span duo-pitch portal frames connected to one another through longitudinal beams at the apex, eaves and bracket levels. While lateral loads are sustained by the MRF system in the transverse direction, the resistance in the longitudinal direction is mainly provided by the diagonal concentric brace members symmetrically placed in the outer spans of the frame (i.e. concentrically braced frame, CBF, at the ground level and cross and sigle braces at the crane-bracket level). As secondary structural elements, purlins, supporting the roof cladding and transferring loads from the roof cladding to the rafters, were also placed on the rafters with a constant interval. Roof cross braces were arranged in the outer bays to transfer lateral loads to the vertical braces. The connection details of the frames are as follows: the full-strength bolted end-plate connections were adopted at the apex and eaves, including haunches to improve the structural performance as well as to facilitate the construction; hinged and pinned connections were adopted for the column-based connections and the purlin-rafter connections, respectively; the brace members were installed through gusset plate connections.

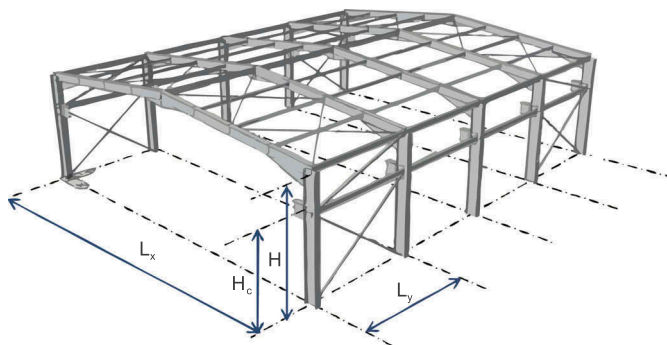


Figure 4 Example of the prototype steel frame buildings.

For each site, four different configurations were considered varying four geometry parameters of the portal frames; i.e. transverse and longitudinal bay widths and story- and crane-bracket heights, denoted as L_X , L_Y , H , and H_c , as provided in Table 1. MRS analysis was performed for seismic design. The design seismic actions in horizontal and vertical directions were obtained from the elastic spectra divided by a q factor equal to 4.0 (for both MRF and CBF systems in low ductility class). In fact, the cross-section designs of structural members for all the combinations of four geometry types (denoted as Geo1-4), three sites, and two soil conditions, resulted in nine different configurations after all, showing that soil condition does not differentiate structural member design. The 3D numerical models were constructed by modeling structural components, including the crane runway beam, by nonlinear beam-column finite elements with fiber sections. For more details of structural design and modeling, see Scozzese et al. (2018).

2.2.4. Industrial PRC Buildings

Single-story industrial PRC buildings were designed at the three sites with different hazard levels (on soil A and C). Each building features 5 one-bay transverse duo-pitched portal frames (i.e. 4×1 bays) consisting of columns and prestressed principal beams, longitudinal beams, prestressed roof elements, and vertical/horizontal cladding panels. Figure 5a,b show the plan and elevation views of the prototype buildings, respectively. The columns were assumed to be fixed at the isolate socket foundation at the base and to be connected at the top to both the transverse and longitudinal beams through dowel connections (CNR 10025/98 2000). The roof system consists of precast π -shaped elements, which are pinned to the beams by means of dowel connections and connected to each other by steel elements in conjunction with a cast-in-situ concrete slab (slab thickness of 50 mm) ensuring the rigid diaphragm assumption. The vertical cladding panels are connected to the beams and columns by means of an interlocking system made of steel elements. Each building, typically intended for industrial use, has an overhead traveling crane (not modeled, but accounted for in design), thus there are precast brackets supporting steel runway beams at some intermediate height of the vertical columns. The beams have variable cross-sections varying width and height along the longitudinal and transversal directions, respectively, while columns have rectangle cross-sections with reinforcing steel bars in two horizontal directions. As with the steel buildings, for each site, four different configurations were considered to represent the typical industrial constructions in Europe, varying four geometry parameters of the frames. Those parameters are summarized in Table 2.

The seismic design of the buildings was performed by means of MRS analysis for two horizontal and vertical directions at each site. The design response spectrum was obtained from the horizontal elastic response spectra (Fig. 1b) divided by a behavior factor $q = 2.5$, which was prescribed by NTC for low ductility class precast buildings with isostatic columns. See Magliulo et al. (2018) for more details of structural design and modeling.

Table 1 Geometry parameters for the prototype steel buildings.

Geometry	L_x [m]	L_y [m]	H [m]	H_c [m]
1	20	6	6	4.5
2	20	8	6	4.5
3	30	6	9	7.5
4	30	8	9	7.5

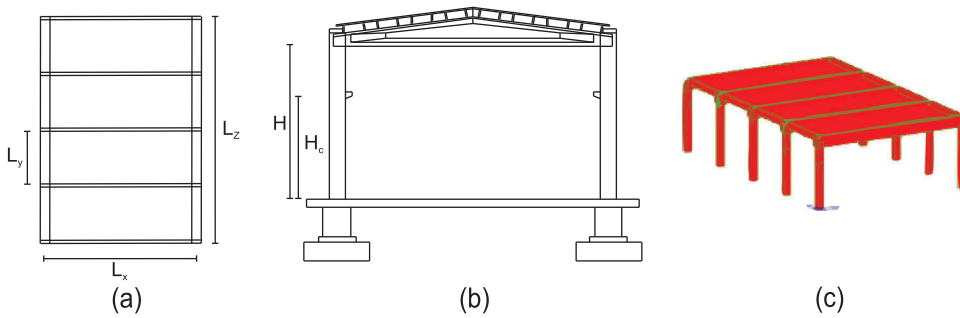


Figure 5 Examples of the prototype PRC buildings; (a) plan view; (b) elevation view; (c) numerical model.

Table 2 Geometry parameters for prototype PRC buildings.

Geometry	L_x [m]	L_y [m]	H [m]	H_c [m]
1	15	6	6	4.5
2	20	8	6	4.5
3	15	6	9	7.5
4	20	8	9	7.5

2.3. Failure Criteria Examined Using 3D Structural Models

The RINTC project assessed structural reliability with respect to the exceedance of two performance levels, global collapse and usability-preventing onset of damage. As this study aims to provide seismic fragility with respect to the former condition only, this section briefly reviews the collapse criteria adopted in the project.

The collapse criteria were in general defined based on the deformation capacity corresponding to a certain level of strength deterioration; i.e. 50% of the maximum base-shear on the static pushover (SPO) curves of the structures for each horizontal direction (Fig. 6). This is the case of the URM, RC and PRC buildings, however, there are some exceptions or adjustments required for some structural typologies, which are explained below.

For the URM buildings, the collapse criteria were defined based on the maximum inter-story drift ratio (IDR) of single-wall elements corresponding to a 50% drop of the maximum base-shear from pushover analysis. For each structure, SPO analysis was carried out under different load patterns (i.e. uniform or inverted triangular) in both horizontal directions, whose minimum value was defined as the collapse limit threshold. Some adjustments were made in the cases the dynamic deformation capacity was found to be lower than the SPO-based threshold value (possibly because of torsional effects and/or cyclic degradation). In particular, the threshold was adjusted to the maximum IDR corresponding to a 35% drop of the maximum base-shear on the static capacity curve (RINTC-Workgroup 2018).

Particularly to PRC buildings, a local collapse condition corresponding to the attainment of the maximum shear strength of the beam-column connections, which is critical for this structural type, was also considered.

Since the prototype steel buildings have different load-resisting systems in two horizontal directions, the collapse criteria were defined individually for each of them: 10% IDR was selected for the direction with the MRF system following indications by FEMA

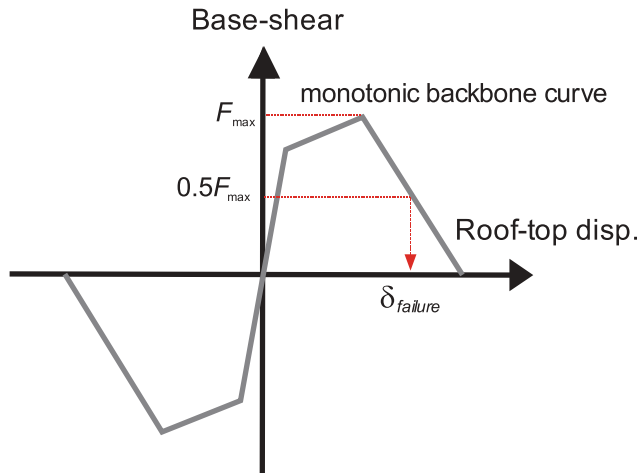


Figure 6 General failure criteria for the prototype buildings.

350 (FEMA 2013), whereas the collapse in the CBF system corresponds to the attainment of the maximum strain range, defined as the difference between minimum and maximum strain responses measured at the cross-sections of brace members under earthquake excitation, equal to 4.9%. For the latter, the strain range threshold was set according to the past studies on local collapse in brace members due to low-cyclic fatigue (Hsiao, Lehman, and Roeder 2013).

It should be mentioned that the coupled responses were considered through the simultaneous input of pairs of horizontal accelerograms to the 3D models and that there were some cases of *numerical instability*, according to Shome and Cornell (2000), observed in dynamic analysis. Thus, *structural failure* was considered to have been reached in cases of numerical instability or the attainment of the collapse criteria in either of the two horizontal directions.

2.4. ESDoF Characterization of the Prototype Buildings

The conversion to an ESDoF model involves the definitions of the SDoF oscillator's characteristics (e.g. the equivalent mass m^* and vibration period T^*) and SPO backbone parameters, and the characterization of the hysteretic behavior. The dynamic and static capacities are first defined based on the SPO curves and the modal contribution of the dominant vibration mode of the original multi (n)-story structural models, then the choice of hysteretic models follows. Figure 7 illustrates the detailed conversion process of the 3D structural models of the prototype buildings to the ESDoF systems. First of all, SPO analysis was carried out per principal direction of each 3D structural model under the modal load distribution; the load profile F_i , which is the product of the floor mass m_i and the dimensionless displacement profile ϕ_i , was applied to each floor level, $i = \{1, 2, \dots, n\}$ (Fig. 7a). The obtained SPO curve was then multi-linearized to characterize the force-displacement relationship of the original structure, opting for bi-linear, tri-linear, and quad-linear fitting depending on the structural type and/or configuration at hand, according to the criteria set forth by De Luca, Vamvatsikos, and Iervolino (2013). Approximating the

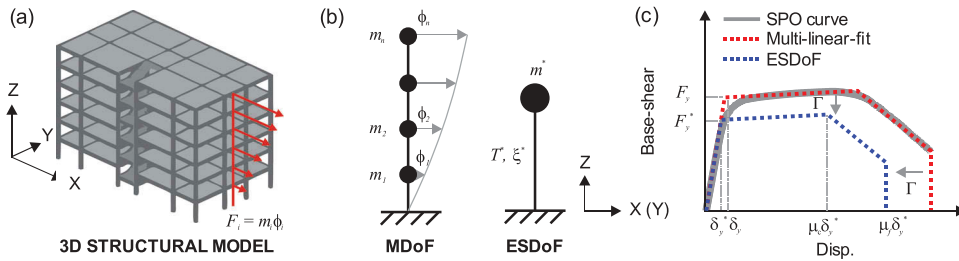


Figure 7 ESDoF conversion; (a) SPO analysis with a 3D model; (b) conversion through lumped mass MDof approximation; (c) characterization of the SPO backbone of the ESDof system.

original frame model with a lumped mass multiple-degree-of-freedom (MDof) system (Fig. 7b), the MDof quantities were subsequently transformed to those of the ESDof system (Fajfar 2000) as follows: the equivalent mass was given by $m^* = \sum_{i=1}^n m_i \phi_i^2$, while the equivalent vibration period T^* was determined as $T^* = 2\pi \sqrt{m^* \delta_y^* / F_y^*}$, where F_y^* and δ_y^* were the yield strength and the yield displacement of the multi-linearized SPO curve (F_y and δ_y , respectively) divided by the modal participation factor, $\Gamma = m^* / \sum_{i=1}^n m_i \phi_i^2$; the yielding spectral acceleration at the equivalent period was then obtained by $Sa_y(T^*) = F_y^* / m^*$; mass- and initial-stiffness-proportional Rayleigh damping models were adopted for all 3D models; this study assigned an equivalent viscous damping ratio (ζ^*) of 3% to the ESDof systems of the URM buildings and 5% for the other three structural types.² The values of ζ^* correspond to the damping ratio which determined the Rayleigh damping model in the range of dominant vibration modes of the original 3D models. Meanwhile, the SPO backbone curve of the ESDof system was derived from the multi-linear-fitted SPO curve scaled down by Γ , maintaining the same dimensionless parameters to characterize the multi-linear backbone, such as the capping-point ductility μ_c and failure ductility μ_f (Fig. 7c). For the given SPO parameters, a hysteresis law that can approximately represent the overall structural response was applied depending on the structural type at hand.

It should be noted that, as far as the examined regular buildings are concerned, no significant torsional responses have been reported in the RINTC project. Therefore, this study examined structural responses in the two horizontal directions independently by defining two uncoupled ESDof systems for each structure. In dynamic analysis, each system, representing a specific direction of the corresponding to the 3D model, is subjected to one of two horizontal components of a GM record. For the URM and RC buildings, longitudinal and transversal directions are denoted as X and Y, respectively, while the opposite (X-transversal, Y-longitudinal) is applied for the rest.

As regards the collapse criteria, the ESDof models retain those adopted for the 3D structural models as long as the corresponding engineering demand parameter (EDP) is a global response measure which can be directly converted to an equivalent quantity. For the structures whose local collapse condition concerns, an alternative or equivalent EDP is introduced (see the following for the details).

2.4.1. URM ESDoF

The ESDoF systems of the selected URM buildings entailed the following assumptions because the rigid floor slab assumption is not applicable: (i) during the modal analysis with the original models, the average response of all the nodes at each floor was considered to represent the displacement profile of the lumped-mass MDoF system (Fig. 7b), and (ii) the floor mass was computed assuming the total floor weights lumped at each floor, in consideration of masonry walls' contribution. Figure 8 shows the SPO backbones (base-shear, F , vs displacement, δ) of the obtained ESDoF systems for the two horizontal directions. In each panel of the figure, the piece-wise linear fitted backbones are shown, compared to the SPO curves of the 3D structural models scaled down by the corresponding modal participation factor, Γ . The end of each backbone indicates the collapse condition defined above.

The SPO curves were obtained assuming inverted-triangular load distribution. The SPO curves received either tri-linear or quadri-linear fit; the curve up to the maximum base-shear (elastic and hardening branches) was first bi-linearly fitted according to the criteria by De Luca, Vamvatsikos, and Iervolino (2013) and then softening and residual strength branches were determined as to capture the exact SPO curve.

Table 3 reports the structural parameters of the ESDoF systems calibrated based on the SPO curves in Fig. 8, for each case study labeled with acronyms indicating the building site, soil condition, configuration type, and adopted analysis method (e.g. MI A/C1 2st/SB). In the table, strength reduction factors with respect to the design accelerations for SLV, R_{SLV} ,

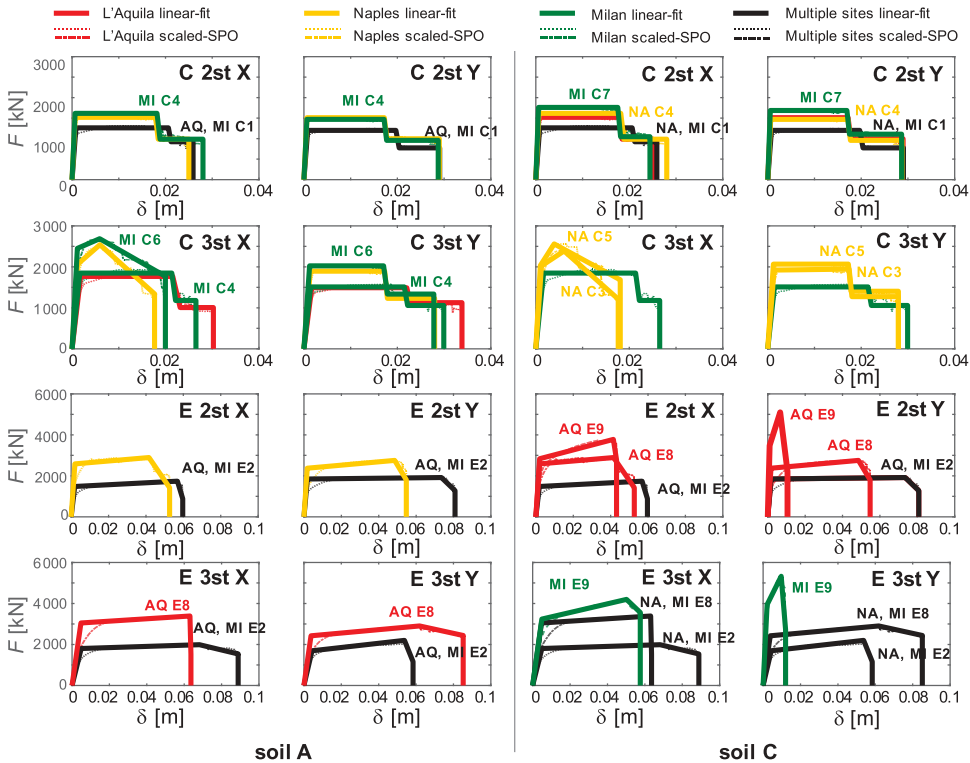


Figure 8 ESDoF-SPO backbones of the C and E-type URM prototype buildings.

Table 3 Structural parameters of ESDoF models of the URM buildings.

Site/config./analysis type	Dir.	F_y [kN]	T_1 [s]	T^* [s]	m^* [ton]	F_y^* [kN]	$Sa_y(T^*)$ [g]	$Sa_{SLV}(T^*)$ [g]	R_{SLV}	μ_f
MI A/C1 2st/SB	X	1542	0.10	0.09	301	1263	0.43	0.12	0.28	31.6
	Y	1513	0.10	0.09	306	1202	0.40	0.12	0.30	36.6
MI A/C4/2st/LSA-F,C	X	1955	0.09	0.07	316	1615	0.52	0.11	0.22	42.4
	Y	1852	0.09	0.08	326	1472	0.46	0.12	0.26	45.3
NA A/C3 2st/SB	X	1855	0.09	0.07	317	1523	0.49	0.31	0.64	38.1
	Y	1888	0.09	0.07	323	1505	0.48	0.31	0.65	45.3
AQ A/C1 2st/NLSA	X	1542	0.10	0.09	301	1263	0.43	0.51	1.18	31.6
	Y	1513	0.10	0.09	306	1202	0.40	0.51	1.26	36.6
MI A/C2 3st/SB	X	2328	0.15	0.14	419	1844	0.45	0.13	0.30	15.9
	Y	2009	0.15	0.13	428	1516	0.36	0.13	0.37	20.9
MI A/C6 3st/LSA-C	X	3013	0.13	0.09	485	2453	0.52	0.13	0.25	17.6
	Y	2672	0.13	0.11	502	2022	0.41	0.13	0.32	22.9
NA A/C4 3st/SB	X	2533	0.14	0.10	456	2057	0.46	0.37	0.81	15.5
	Y	2501	0.14	0.11	472	1894	0.41	0.39	0.96	20.5
AQ A/C1/3st/NLSA	X	2209	0.15	0.13	398	1770	0.45	0.62	1.36	16.4
	Y	1954	0.15	0.13	406	1490	0.37	0.62	1.65	20.1
MI A/E2 2st/LSA-C	X	1811	0.12	0.13	322	1481	0.47	0.13	0.28	31.7
	Y	2244	0.10	0.11	322	1846	0.58	0.13	0.23	44.6
NA A/E8 2st/SB	X	3112	0.12	0.12	476	2584	0.55	0.40	0.72	26.4
	Y	2851	0.10	0.12	475	2373	0.51	0.40	0.78	31.3
AQ A/E2 2st/SB	X	1811	0.12	0.13	322	1481	0.47	0.62	1.32	31.7
	Y	2244	0.10	0.11	322	1846	0.58	0.60	1.03	44.6
MI A/E2 3st/LSA-C	X	2344	0.18	0.22	433	1801	0.42	0.13	0.31	18.1
	Y	2205	0.16	0.21	425	1693	0.41	0.13	0.33	13.6
AQ A/E2 3st/NLSA	X	2344	0.18	0.22	433	1801	0.42	0.62	1.46	18.1
	Y	2205	0.16	0.21	425	1693	0.41	0.62	1.52	13.6
AQ A/E8 3st/NLSA	X	3927	0.19	0.20	626	3049	0.50	0.62	1.24	13.4
	Y	3125	0.16	0.20	616	2422	0.40	0.62	1.54	16.3
MI C/C1 2st/SB	X	1542	0.10	0.09	301	1263	0.43	0.14	0.33	31.6
	Y	1513	0.10	0.09	306	1202	0.40	0.14	0.35	36.6
MI C/C7 2st/LSA-F	X	2148	0.08	0.07	357	1764	0.50	0.13	0.25	42.6
	Y	2125	0.08	0.07	365	1689	0.47	0.13	0.27	51.6
NA C/C1 2st/NLSA	X	1542	0.10	0.09	301	1263	0.43	0.41	0.95	31.6
	Y	1513	0.10	0.09	306	1202	0.40	0.41	1.01	36.6
NA C/C4 2st/SB	X	1955	0.09	0.07	316	1615	0.52	0.39	0.74	42.4
	Y	1852	0.09	0.08	326	1472	0.46	0.41	0.88	45.3
AQ C/C3 2st/NLSA	X	1855	0.09	0.07	317	1523	0.49	0.54	1.10	38.1
	Y	1888	0.09	0.07	323	1505	0.48	0.54	1.14	45.3
MI C/C2 3st/SB	X	2328	0.15	0.14	419	1844	0.45	0.19	0.43	15.9
	Y	2009	0.15	0.13	428	1516	0.36	0.18	0.51	20.9
NA C/C3 3st/NLSA	X	2510	0.14	0.10	460	2017	0.45	0.45	1.00	14.6
	Y	2536	0.14	0.11	466	1920	0.42	0.47	1.11	20.5
NA C/C5 3st/SB	X	2520	0.13	0.10	489	2028	0.42	0.45	1.05	18.7
	Y	2727	0.13	0.11	499	2065	0.42	0.47	1.10	23.1
MI C/E2 2st/LSA-F	X	1811	0.12	0.13	322	1481	0.47	0.18	0.39	31.7
	Y	2244	0.10	0.11	322	1846	0.58	0.17	0.29	44.6
AQ C/E2 2st/NLSA	X	1811	0.12	0.13	322	1481	0.47	0.71	1.51	31.7
	Y	2244	0.10	0.11	322	1846	0.58	0.65	1.11	44.6
AQ C/E8 2st/NLSA	X	3112	0.12	0.12	476	2584	0.55	0.68	1.23	26.4
	Y	2851	0.10	0.12	475	2373	0.51	0.68	1.33	31.3
AQ C/E9 2st/NLSA	X	3386	0.12	0.12	535	2832	0.54	0.68	1.26	21.5
	Y	4112	0.07	0.08	557	3483	0.64	0.57	0.89	10.4
MI C/E2 3st/LSA-F	X	2344	0.18	0.22	433	1801	0.42	0.20	0.47	18.1
	Y	2205	0.16	0.21	425	1693	0.41	0.20	0.49	13.6
MI C/E8 3st/LSA-C	X	3927	0.19	0.20	626	3049	0.50	0.20	0.40	13.4
	Y	3125	0.16	0.20	616	2422	0.40	0.20	0.50	16.3
MI C/E9 3st/SB, LSA-F,C	X	4165	0.18	0.20	703	3240	0.47	0.20	0.42	11.7
	Y	4929	0.11	0.12	752	3942	0.53	0.18	0.33	5.6
NA C/E2 3st/SB, NLSA	X	2344	0.18	0.22	433	1801	0.42	0.58	1.38	18.1
	Y	2205	0.16	0.21	425	1693	0.41	0.58	1.43	13.6
NA C/E8 3st/NLSA	X	3927	0.19	0.20	626	3049	0.50	0.58	1.17	13.4
	Y	3125	0.16	0.20	616	2422	0.40	0.58	1.45	16.3

defined as the ratio of the horizontal elastic spectral acceleration at T^* to the yield acceleration, $Sa_{SLV}(T^*)/Sa_y(T^*)$, are also provided. The summary of design structural parameters shows that the equivalent period of vibration T^* ranges between approximately 0.1–0.2 s and that R_{SLV} increases with the increasing hazard at the site, reflecting the analysis methods adopted for the design. It should be also noted that the first vibration period in the direction of interest, T_1 , was derived from the eigenvalue analysis of the corresponding original 3D model and does not necessarily coincide with the equivalent period, T^* , which was derived through defining the elastic branch up to the point where the scant stiffness reduced by less than 30% of the initial stiffness.

It is worth to mention that the ESDoF systems corresponding to the URM structures were analyzed using OpenSees. Two different hysteresis rules were selected from those available in the OpenSees material library to capture the main collapse mechanisms of the structures under consideration: (1) *flag-shaped* (Christopoulos et al. 2008; Tremblay, Lacerte, and Christopoulos 2008) with moderate energy dissipation and (2) *peak-oriented* (Altoontash 2004) without cyclic strength/stiffness deterioration. The hysteresis rule (1) was opted, even though it was originally intended for self-centering energy dissipative bracing systems, based on the hysteresis response of the original models under cyclic loading that showed a flexure-dominated structural behavior, while (2) was found to capture well the shear-dominated dynamic hysteresis responses of some original models. It should be noted that one of flexure-, shear-, or mixed- type hysteresis models was assigned to each masonry panel of the 3D structural models, depending on the collapse mechanism associated with the geometry of the panel. The computed ESDoF systems will be further verified in terms of dynamic structural response in the following section.

2.4.2. RC ESDoF

The ESDoF systems of the RC buildings were constructed on the basis of rigid floor diaphragm and lumped floor mass assumptions. Figure 9 shows the SPO backbones of the obtained ESDoF systems for the two horizontal directions. In each panel, the piecewise-linear-fitted backbones are shown, compared to the SPO curves of the 3D structural models scaled down by the corresponding modal participation factor, Γ . For the structures with the same number of stories, their static load capacity increases with the increasing site hazard, and IF and PF have higher strength and stiffness than BF due to the additional lateral strength provided by the infill walls. The structural parameters of the ESDoF systems were determined through the tri-linear or quadri-linear idealization of each SPO backbone via a Monte-Carlo-based optimization approach (Baltzopoulos et al. 2017). The structural parameters are summarized in Table 4 for each configuration; T^* varies between 0.2 and 2.1s (the shortest: 3st IF; the longest: 9st BF); the computed R_{SLV} factor ranges from 0.3 to 3.7 showing the same increasing trend with the site hazard as observed for the URM buildings. For the given SPO parameters, a moderately pinching, peak-oriented hysteretic behavior without any cyclic stiffness/strength deterioration, e.g. (Vamvatsikos and Cornell 2006), was applied. For more detailed information on structural features, see Suzuki, Baltzopoulos, and Iervolino (2018).

2.4.3. Steel ESDoF

The industrial steel buildings are all single-story frames, hence the ESDoF systems were constructed based on the unscaled static capacity curves. Since each portal frame behaves

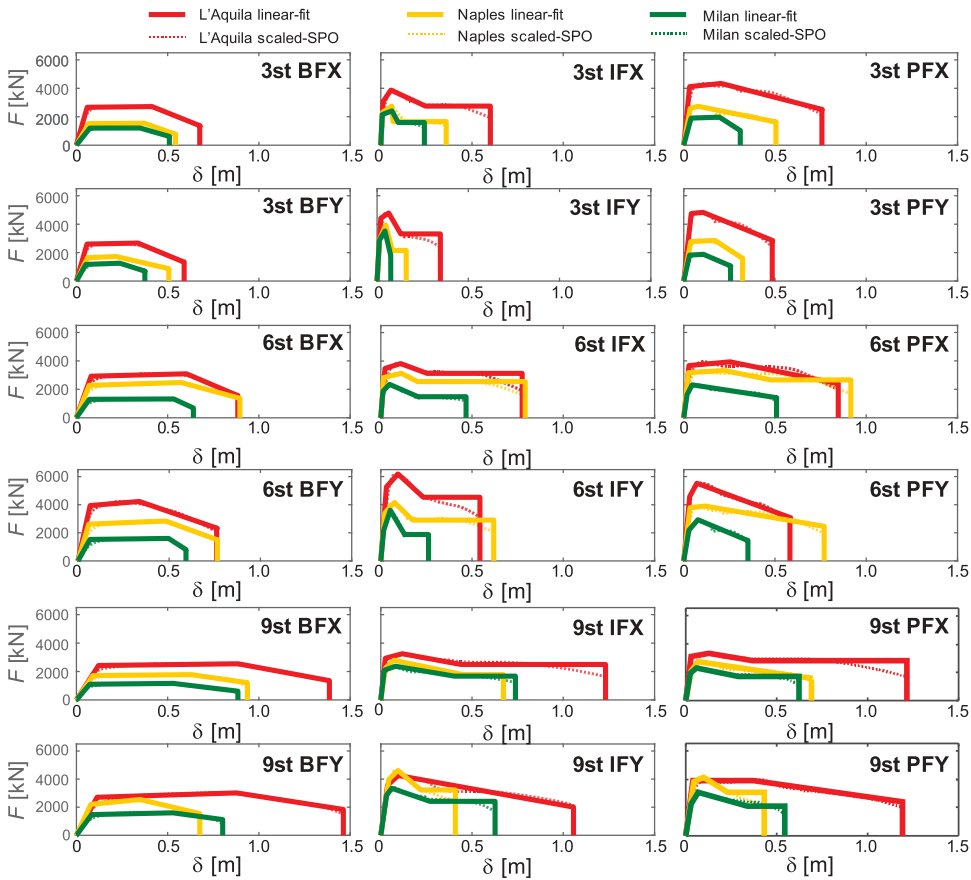


Figure 9 ESDoF-SPO backbones of the prototype RC buildings.

individually due to the absence of a rigid roof diaphragm, the SPO curves were obtained from the roof-top and column-top displacement responses of the intermediate frame in X and Y directions, respectively. [Figure 10a](#) and [Table 5](#) show the SPO backbones and the structural parameters of the obtained ESDoF systems (each was designed for both the soil conditions A and C). Each SPO curve received bi-linear fitting (similar to URM) up to the maximum strength, then the softening phase was added in case the curve indicates strength deterioration. Reflecting the different load-resisting systems in the two horizontal directions, each structure exhibits the higher resistance capacity in the X direction and the shorter vibration period in the Y direction. Moreover, it can be observed that the capacities of the structures with the same configuration are nearly identical, in spite of the different hazard levels at the three sites, thus resulting in the clear trend of the increasing R_{SLV} factors with hazard. Given the characteristics of each load-bearing system, a bilinear hysteresis model (Ibarra, Medina, and Krawinkler 2005) and moderately pinching peak-oriented hysteresis model (the same for RC buildings), both without any cyclic stiffness/strength deterioration, were applied in the X and Y directions, respectively. As an equivalent response measure of the collapse in the brace members, this study investigated three possible global quantities. Assuming that the static strain capacity of the brace

Table 4 Structural parameters of the multiple-story RC buildings.

Site/config.	Dir.	F_y [kN]	T_1 [s]	T^* [s]	m^* [ton]	F_y^* [kN]	$Sa_y(T^*)$ [g]	$Sa_{SLV}(T^*)$ [g]	R_{SLV}	μ_f
MI C/BF 3st	X	1542	1.04	1.10	497	1201	0.25	0.08	0.33	6.9
	Y	1492	0.90	0.95	508	1171	0.23	0.09	0.40	7.2
NA C/BF 3st	X	1959	0.89	0.93	496	1520	0.31	0.32	1.02	8.0
	Y	2100	0.83	0.86	510	1643	0.33	0.34	1.05	8.3
AQ C/BF 3st	X	3455	0.66	0.68	534	2668	0.51	0.62	1.22	11.4
	Y	3344	0.67	0.69	543	2600	0.49	0.61	1.26	10.2
MI C/IF 3st	X	2718	0.21	0.27	517	2154	0.43	0.20	0.47	30.1
	Y	3584	0.24	0.30	524	2851	0.56	0.20	0.36	6.0
NA C/IF 3st	X	2898	0.22	0.28	531	2302	0.44	0.58	1.32	40.3
	Y	3642	0.24	0.31	538	2907	0.55	0.58	1.06	12.3
AQ C/IF 3st	X	3839	0.23	0.30	580	3059	0.54	0.82	1.53	50.2
	Y	5514	0.25	0.33	590	4422	0.76	0.82	1.08	17.1
MI C/PF 3st	X	1956	0.74	0.76	701	1905	0.28	0.12	0.42	7.8
	Y	1891	0.67	0.69	693	1821	0.27	0.13	0.48	8.1
NA C/PF 3st	X	2709	0.60	0.62	703	2594	0.38	0.48	1.27	14.2
	Y	2912	0.60	0.62	700	2776	0.40	0.48	1.18	8.5
AQ C/PF 3st	X	4506	0.43	0.47	730	4119	0.58	0.82	1.43	23.5
	Y	5198	0.50	0.50	731	4754	0.66	0.82	1.24	11.8
MI C/BF 6st	X	1658	1.70	1.70	1245	1299	0.11	0.05	0.49	9.1
	Y	1924	1.48	1.48	1283	1529	0.12	0.06	0.50	9.0
NA C/BF 6st	X	2935	1.25	1.25	1306	2283	0.18	0.24	1.33	12.8
	Y	3300	1.11	1.11	1376	2618	0.19	0.27	1.37	12.9
AQ C/BF 6st	X	3829	1.13	1.13	1177	2923	0.25	0.38	1.48	11.0
	Y	5246	0.88	0.87	1147	3941	0.35	0.49	1.39	11.4
MI C/IF 6st	X	2458	0.53	0.53	1161	1865	0.16	0.17	1.03	41.1
	Y	2874	0.58	0.58	1165	2164	0.19	0.15	0.81	16.5
NA C/IF 6st	X	3714	0.52	0.53	1265	2842	0.23	0.56	2.43	50.5
	Y	4493	0.57	0.57	1262	3419	0.28	0.52	1.88	28.0
AQ C/IF 6st	X	4544	0.51	0.57	1230	3485	0.29	0.74	2.57	33.6
	Y	6827	0.50	0.54	1247	5269	0.43	0.78	1.82	17.6
MI C/PF 6st	X	1874	0.92	0.92	1616	1636	0.10	0.10	0.94	27.7
	Y	2597	0.88	0.88	1533	2184	0.15	0.10	0.70	12.7
NA C/PF 6st	X	3874	0.69	0.69	1560	3170	0.21	0.43	2.07	37.2
	Y	4672	0.73	0.73	1530	3787	0.25	0.40	1.58	22.4
AQ C/PF 6st	X	4616	0.60	0.65	1401	3671	0.27	0.65	2.44	30.0
	Y	6080	0.54	0.57	1251	4581	0.37	0.74	2.10	17.9
MI C/BF 9st	X	1451	2.12	2.09	1684	1105	0.07	0.04	0.55	12.2
	Y	1944	1.93	1.93	1677	1472	0.09	0.04	0.48	9.6
NA C/BF 9st	X	2262	1.88	1.92	1763	1711	0.10	0.15	1.56	10.3
	Y	2972	1.55	1.56	1721	2208	0.13	0.19	1.45	8.5
AQ C/BF 9st	X	3181	1.86	1.86	1774	2423	0.14	0.23	1.64	11.4
	Y	3639	1.67	1.68	1725	2707	0.16	0.25	1.58	12.9
MI C/IF 9st	X	2811	0.77	0.77	1639	2094	0.13	0.12	0.89	38.1
	Y	3892	0.84	0.84	1591	2846	0.18	0.11	0.58	19.5
NA C/IF 9st	X	2941	0.89	0.90	1829	2228	0.12	0.33	2.64	26.9
	Y	5329	0.88	0.89	1792	3983	0.23	0.33	1.47	9.3
AQ C/IF 9st	X	3844	0.76	0.78	1728	2936	0.17	0.54	3.14	48.8
	Y	4874	0.84	0.84	1695	3589	0.22	0.50	2.34	28.1
MI C/PF 9st	X	2423	0.97	0.97	2011	1898	0.10	0.09	0.95	27.3
	Y	2945	1.00	1.00	1886	2232	0.12	0.09	0.74	18.0
NA C/PF 9st	X	2723	0.99	1.00	2012	2106	0.11	0.30	2.77	25.8
	Y	5082	0.94	0.95	1917	3847	0.21	0.31	1.52	9.3
AQ C/PF 9st	X	4077	0.89	0.87	2012	3140	0.16	0.49	3.06	40.2
	Y	5148	0.89	0.89	1853	3859	0.21	0.48	2.24	28.9

members under monotonic loading can somewhat indicate the dynamic one, the first two were the displacements on the SPO curve corresponding to a brace strain (ϵ) of (1) 4.9% and (2) 2.45% (the equivalent strain ranges under monotonic loading and under ideally symmetric loading; $\delta_{f,\epsilon=4.9\%}$ and $\delta_{f,\epsilon=2.45\%}$, respectively). As illustrated in Fig. 10b, the

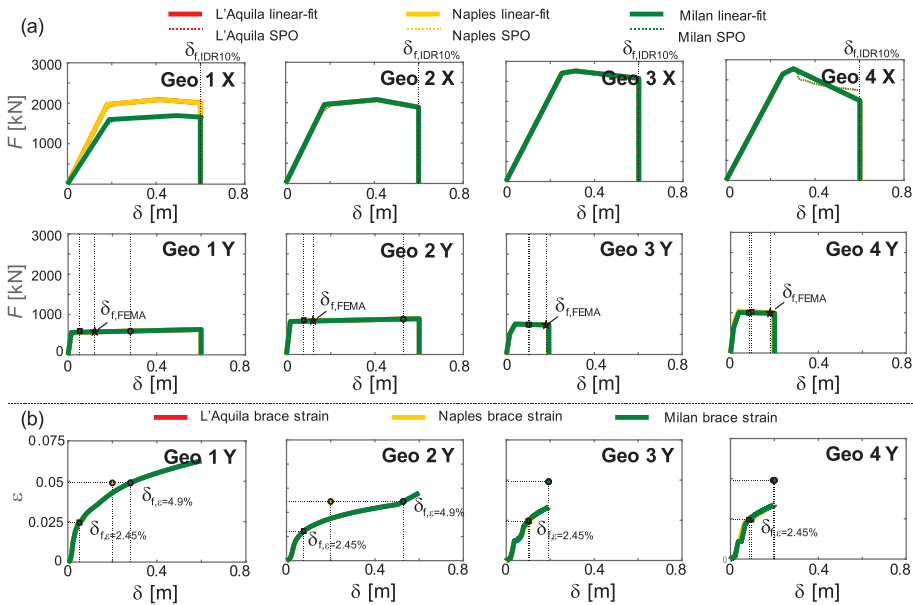


Figure 10 ESDoF-SPO backbones of the prototype steel buildings and brace-strain-displacement curves.

brace strain responses were also monitored in pushover analysis, then those strain thresholds were translated into the corresponding displacements (only when available). The third was a displacement corresponding to (3) 2.0% transient IDR suggested by FEMA 356 (ASCE, 2000) for collapse prevention performance level of braced steel frames, $\delta_{f,FEMA}$. The three of them are also indicated together with the capacity curves in Fig. 10a,b, as well as the displacement limit values, $\delta_{f,IDR10\%}$ in the X direction.

2.4.4. PRC ESDoF

As with the steel buildings, the ESDoF systems of the PRC buildings were constructed directly based on the unscaled static capacity curves assuming a lumped mass and rigid diaphragm at the roof level. Figure 11 shows the SPO backbones of the obtained ESDoF systems for the two horizontal directions. In fact, the SPO curves of the original structural models exhibited the multi-linear backbones owing to its modeling approaches, thus the ESDoF systems retain the exact SPO curves without any fitting. The SPO curve of each system consists of three segments (elastic-hardening-softening), whose endpoint corresponds to the displacement-based collapse criterion defined above. As it regards the local collapse criterion for the beam-column connection, the ratio of the maximum base-shear recorded in dynamic analysis and connection shear capacity reported in Magliulo et al. (2018) was considered as an alternative response measure. As seen in the figure, structural resistance varies across the different configurations and hazard levels at the sites, while the deformation capacity does not change significantly among the four configurations. The computed structural parameters for all considered cases are summarized in Table 6; T^* ranges between 1.2 and 2.4 s and the computed R_{SLV} factors resulted to be smaller than 1 for all cases. The peak-oriented hysteretic behavior

Table 5 Structural parameters of the steel buildings.

Site/config.	Dir.	T_1 [s]	T^* [s]	m^* [ton]	F_y^* [kN]	$Sa_y(T^*)$ [g]	Soil A		Soil C		μ_f
							$Sa_{SLV}(T^*)$ [g]	R_{SLV}	$Sa_{SLV}(T^*)$ [g]	R_{SLV}	
MI/Geo 1	X	0.67	0.59	73	1597	2.22	0.06	0.03	0.15	0.07	3.2
	Y	0.32	0.27	73	557	0.77	0.12	0.17	0.20	0.26	-
NA/Geo 1	X	0.60	0.51	73	1967	2.73	0.26	0.10	0.58	0.21	3.4
	Y	0.30	0.27	73	557	0.77	0.40	0.52	0.58	0.75	-
AQ/Geo 1	X	0.60	0.51	73	1967	2.73	0.42	0.15	0.82	0.30	3.4
	Y	0.32	0.27	73	557	0.77	0.62	0.80	0.82	1.06	-
MI/Geo 2	X	0.66	0.58	95	1956	2.10	0.06	0.03	0.15	0.07	3.4
	Y	0.35	0.35	95	820	0.88	0.11	0.12	0.20	0.23	-
NA/Geo 2	X	0.66	0.58	95	1956	2.10	0.23	0.11	0.51	0.24	3.4
	Y	0.34	0.28	95	820	0.88	0.40	0.45	0.58	0.66	-
AQ/Geo 2	X	0.66	0.58	95	1956	2.10	0.37	0.17	0.73	0.35	3.4
	Y	0.35	0.28	95	820	0.88	0.61	0.69	0.82	0.93	-
MI/Geo 3	X	0.79	0.63	108	2707	2.56	0.06	0.02	0.14	0.06	2.4
	Y	0.37	0.35	108	503	0.48	0.11	0.22	0.20	0.42	-
NA/Geo 3	X	0.79	0.63	108	2707	2.56	0.21	0.08	0.47	0.18	2.4
	Y	0.38	0.35	108	503	0.48	0.39	0.81	0.58	1.23	-
AQ/Geo 3	X	0.79	0.63	108	2707	2.56	0.34	0.13	0.67	0.26	2.4
	Y	0.37	0.35	108	503	0.48	0.61	1.29	0.82	1.73	-
MI/Geo 4	X	0.85	0.70	130	2645	2.07	0.05	0.03	0.13	0.06	2.4
	Y	0.38	0.33	130	628	0.49	0.11	0.23	0.20	0.41	-
NA/Geo 4	X	0.85	0.70	130	2645	2.07	0.20	0.09	0.43	0.21	2.4
	Y	0.37	0.33	130	781	0.61	0.40	0.65	0.58	0.95	-
AQ/Geo 4	X	0.85	0.70	130	2645	2.07	0.31	0.15	0.61	0.30	2.4
	Y	0.38	0.33	130	628	0.49	0.62	1.26	0.82	1.67	-

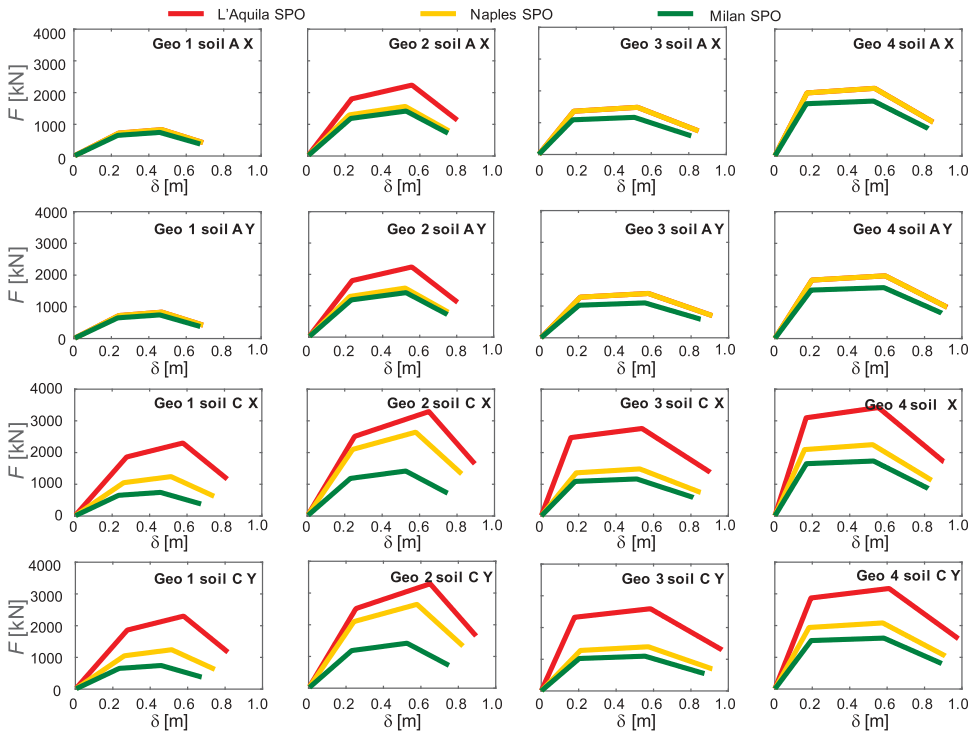


Figure 11 ESDoF-SPO backbones of the prototype PRC buildings.

Table 6 Structural parameters of the PRC buildings.

Site/config.	Dir.	T_1 [s]	T^* [s]	m^* [ton]	F_y^* [kN]	$Sa_y(T^*)$ [g]	$Sa_{SLV}(T^*)$ [g]	R_{SLV}	μ_f
MI A/Geo 1	X	2.28	2.37	398	654	0.17	0.01	0.07	2.88
	Y	2.28	2.37	398	654	0.17	0.01	0.07	2.88
NA A/Geo 1	X	2.20	2.28	398	725	0.19	0.06	0.32	2.88
	Y	2.20	2.28	398	725	0.19	0.06	0.32	2.88
AQ A/Geo 1	X	2.20	2.28	398	724	0.19	0.09	0.51	2.88
	Y	2.20	2.28	398	741	0.19	0.09	0.50	2.82
MI A/Geo 2	X	2.02	2.08	566	1186	0.21	0.02	0.08	3.25
	Y	2.02	2.08	566	1186	0.21	0.02	0.08	3.25
NA A/Geo 2	X	1.91	1.96	566	1299	0.23	0.07	0.29	3.39
	Y	1.91	1.96	566	1298	0.23	0.07	0.29	3.39
AQ A/Geo 2	X	1.68	1.71	566	1804	0.33	0.13	0.39	3.40
	Y	1.68	1.71	566	1804	0.33	0.13	0.39	3.42
MI A/Geo 3	X	1.78	1.84	515	1091	0.22	0.02	0.09	4.49
	Y	1.94	2.01	515	1024	0.20	0.02	0.08	4.19
NA A/Geo 3	X	1.63	1.67	515	1361	0.27	0.08	0.29	4.56
	Y	1.78	1.83	515	1278	0.25	0.07	0.29	4.35
AQ A/Geo 3	X	1.63	1.67	515	1361	0.27	0.13	0.46	4.56
	Y	1.78	1.83	515	1278	0.25	0.12	0.46	4.36
MI A/Geo 4	X	1.74	1.80	802	1650	0.21	0.02	0.10	4.86
	Y	1.94	2.01	802	1528	0.19	0.02	0.08	4.59
NA A/Geo 4	X	1.61	1.66	802	1991	0.25	0.08	0.32	4.91
	Y	1.79	1.85	802	1844	0.23	0.07	0.31	4.64
AQ A/Geo 4	X	1.29	1.66	802	1990	0.25	0.13	0.50	4.91
	Y	1.44	1.85	802	1843	0.23	0.11	0.49	4.65
MI C/Geo 1	X	2.28	2.37	398	654	0.17	0.03	0.17	2.88
	Y	2.28	2.37	398	654	0.17	0.03	0.17	2.88
NA C/Geo 1	X	1.91	1.98	398	1052	0.27	0.15	0.55	2.85
	Y	1.91	1.98	398	1052	0.27	0.15	0.55	2.85
AQ C/Geo 1	X	1.51	1.53	398	1865	0.48	0.28	0.58	2.93
	Y	1.51	1.53	398	1865	0.48	0.28	0.58	2.93
MI C/Geo 2	X	2.02	2.08	566	1186	0.21	0.04	0.17	3.25
	Y	2.02	2.08	566	1186	0.21	0.04	0.17	3.25
NA C/Geo 2	X	1.58	1.61	566	2103	0.38	0.18	0.48	3.40
	Y	1.58	1.61	566	2103	0.38	0.18	0.48	3.40
AQ C/Geo 2	X	1.48	1.50	566	2513	0.45	0.28	0.62	3.53
	Y	1.48	1.50	566	2513	0.45	0.28	0.62	3.53
MI C/Geo 3	X	1.78	1.84	515	1091	0.22	0.05	0.21	4.49
	Y	1.94	2.05	515	1024	0.20	0.04	0.19	4.29
NA C/Geo 3	X	1.63	1.67	515	1361	0.27	0.17	0.64	4.56
	Y	1.78	1.86	515	1278	0.25	0.16	0.63	4.36
AQ C/Geo 3	X	1.16	1.17	543	2473	0.46	0.35	0.76	5.70
	Y	1.26	1.31	543	2324	0.44	0.32	0.74	5.44
MI C/Geo 4	X	1.74	1.80	802	1656	0.21	0.05	0.23	4.84
	Y	1.94	2.01	802	1527	0.19	0.04	0.20	4.59
NA C/Geo 4	X	1.52	1.56	812	2094	0.26	0.19	0.71	5.27
	Y	1.70	1.74	812	1940	0.24	0.17	0.69	4.98
AQ C/Geo 4	X	1.61	1.31	802	3097	0.39	0.32	0.80	5.39
	Y	1.79	1.46	802	2870	0.36	0.28	0.78	5.08

model embedded into the column hinges of the original models (Ibarra, Medina, and Krawinkler 2005) was considered in this study, however no cyclic stiffness/strength deterioration was assumed unlike the original models.

To close this section, Fig. 12 shows the hysteresis loops under cyclic loading for some representative cases of each structural type.

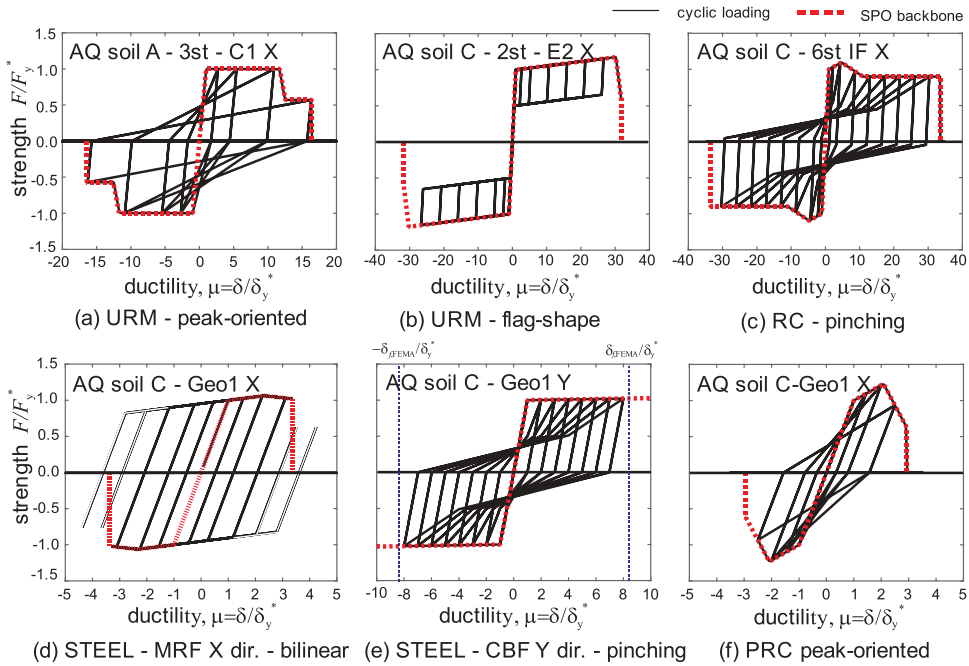


Figure 12 Hysteresis laws for the prototype buildings.

3. Structural Model Verification

This section verifies the approximation of the computed ESDoF models, which will be used to develop fragility functions in the next section. For some representative cases, the structural responses in terms of demand-capacity (D/C) ratio of the corresponding EDP, which was computed in the same manner as the RINTC project, are compared with those obtained from the original 3D structural models (RINTC-Workgroup 2018). The following first briefly recalls the RINTC risk assessment scheme, followed by the comparisons of the D/C ratios.

3.1. RINTC Risk Assessment Scheme

In the PBEE framework, the seismic risk of a structure is commonly quantified as the expected number in 1 year of earthquakes capable to cause structural failure; i.e. *failure rate*, λ_f . This is obtained through integrating a probabilistic representation of seismic vulnerability and probabilistic seismic hazard, which is expressed as:

$$\lambda_f = \int_x P[failure|IM = x] d\lambda_x \tag{1}$$

In the equation, seismic vulnerability is represented as a function providing the failure probability conditional to the values (x) of an IM, $P[failure|IM = x]$, while hazard is expressed by means of the annual rate of exceeding the x values, λ_x , computed through probabilistic seismic hazard analysis (PSHA) (Cornell 1968).

In the RINTC project, the term $P[\text{failure}|IM = x]$ in Eq. (1) was computed through MSA with the 3D nonlinear structural (MDoF) models at 10 IM levels (IMLs), $IM = x_i$ where $i = \{1, 2, \dots, 10\}$, corresponding to exceedance return periods of $T_{R,i} = \{10, 50, 100, 250, 500, 1000, 2500, 5000, 10000, 100000\}$ years, up to which PSHA was carried out for each site (the risk integral with the truncated hazard will be discussed in the following section).

In the project, hazard curves were computed for the pseudo-acceleration spectral ordinates at the periods $T = \{0.15\text{s}, 0.5\text{s}, 1.0\text{s}, 1.5\text{s}, 2.0\text{s}\}$, which cover the range of the first-mode vibration periods of the 3D models (approximately between 0.10s-2.3s; see Table 3–6). Then, the spectral acceleration, $Sa(T)$, at the period closest to the first-mode period was selected as the IM to condition GM records for response assessment. (The conditioning period closest to the structural fundamental period in the X direction was chosen for the steel buildings whose fundamental periods of vibration have a range between the two horizontal directions.) For each site, record selection was hazard-consistent by means of the conditional spectrum (CS) approach (Kohrangi, Vamvatsikos, and Bazzurro 2017; Lin, Haselton, and Baker 2013) collecting 20 GM records for each IML of the selected IM. See Iervolino, Spillatura, and Bazzurro (2018) for the record selection procedure and Suzuki (2019) for the complete sets of the GM records.

3.2. ESDoF vs. MDoF Responses

MSA was performed using the calibrated ESDoF systems following the structural analysis strategy adopted in the RINTC project. The D/C ratios were computed by taking the ratios of the measured EDP values to the defined capacity based on the pushover curve of the structure (or based on the FEMA 356 recommendations for steel buildings). Figure 13 shows the measured D/C ratios at the 10 IMLs, as well as the numbers of failure cases ($N_{f,IM=x_i}$, with the lowercase letters representing the corresponding system) out of the total number of records, $N_{tot,IM=x_i} = 20$, for some representative cases of each structural type and/or configuration. The buildings designed at the most severe hazard site of the three sites, AQ, are chosen for the sake of illustration. Figure 13a,b show the results for two cases of the URM buildings, the three-story C-type (C1, soil A) and the two-story E-type building (E2, soil C), respectively. The ESDoF models assume either flexure- or shear-dominated hysteresis response unlike the original 3D models (denoted as cross markers in the figure) where the response is mixed considering the contributions from multiple masonry panels. For this reason, the figures show the larger value of the D/C ratios between the flexure- and shear-dominated hysteresis, indicated with F and S subscripts respectively, models for each (j) GM record, $j = \{1, 2, \dots, N_{tot,IM=x_i}\}$, at each (i) IML, $D/C = \max(D/C_{F,i,j}, D/C_{S,i,j})$. It is observed that the ESDoF responses succeeded to capture the trends of the original 3D models (black cross markers) and the number of failure cases over the IMLs, especially for the C-type buildings, however, resulted in some underestimation, especially at the intermediate IMLs for the E-type buildings. This is possibly because: (1) the considered EDP for the original models, that is the maximum IDR of the single-wall elements, is larger than the corresponding roof drift considered for the ESDoFs when a soft story collapse mechanism occurs; (2) the actual tangent stiffness of the exact pushover curve of each E-type building, corresponding to the

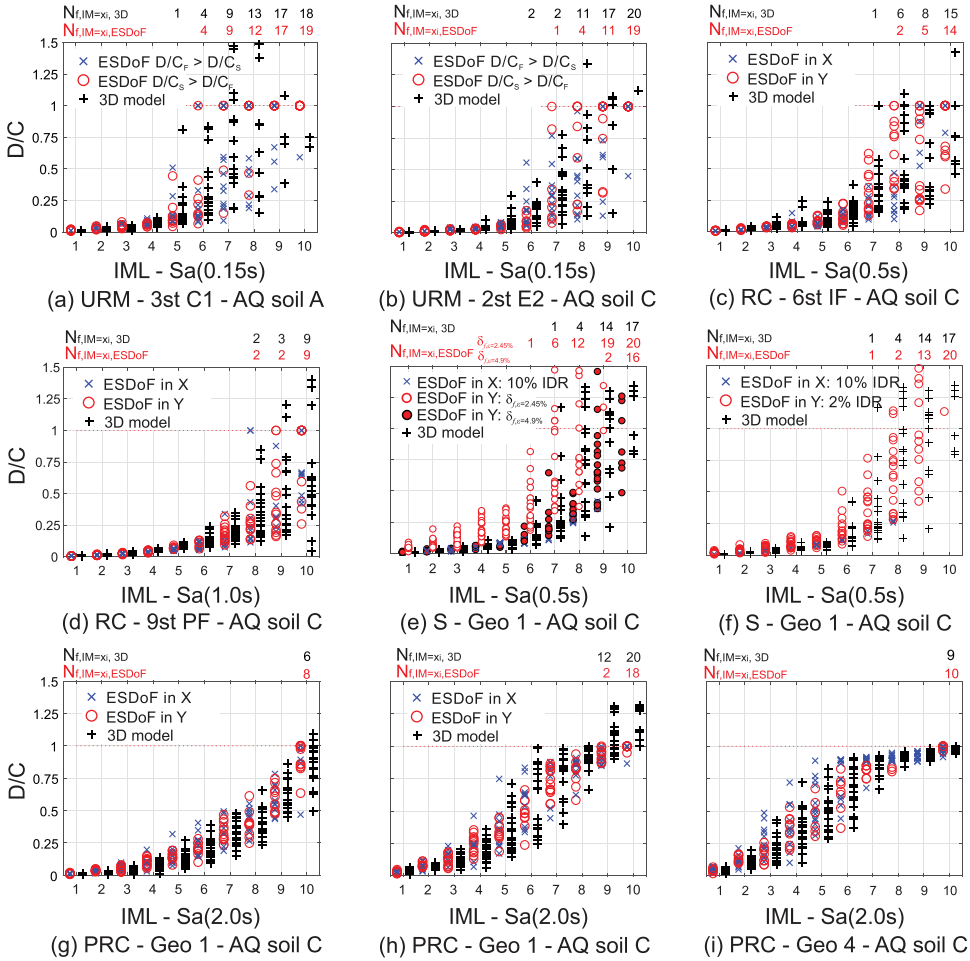


Figure 13 Comparisons of D/C ratios.

elastic branch of the multi-fitted SPO, reduces from the equivalent stiffness (see Fig. 8 and Section 2.4.1).

Figure 13c,d show the results for two cases of the RC buildings, six-story IF and nine-story PF buildings, respectively. The D/C ratios are shown in the figures with colored markers to distinguish the principal direction which led to the larger value of the D/C ratio and are compared to those from the original 3D models. As seen in the presented cases, the computed D/C ratios and the number of failure cases have good agreement between the two structural systems, in most cases, over the multiple IMLs. Figure 13e,f represents the results for the steel building with Geo 1 (AQ on soil C). As reported in the study with the original 3D models, the D/C ratios at the larger IMLs mostly come from the longitudinal (Y) direction associated with the failure in the brace members. Consistently, the D/C ratios computed from the ESDoF systems significantly varied depending on the considered candidate global response measures. Among those, the displacement limit values associated with the static local strain capacities, $\delta_{f,\varepsilon=4.9\%}$ and $\delta_{f,\varepsilon=2.45\%}$ did not agree with the observed responses of the frame models under earthquake excitation,

indicating the inadequacy of these measures for predicting the failure in the brace members (Fig. 13e). On the other hand, 2.0% IDR suggested by FEMA 356, $\delta_{f,FEMA}$, (Fig. 13f) resulted in the best estimates of the D/C ratios in most of the cases, although some may argue it is not comparable with the strain-based EDP for the original frame models.

Figure 13g–i show the computed D/C ratios for the PRC buildings of Geo 1 and 4 (AQ soil C) with respect to the displacement-based global collapse criteria and the force-based ones associated with the connection failure. Both the approaches (i.e. displacement-based and force-based) somewhat agree with the original models for all considered cases (e.g. Fig.s 13g,i), except the force-based approach for Geo 1 and 2 (e.g. Fig. 13h). This is because, in fact, the original structural models of these configurations assumed the mass distributed at the connection- and crane-bracket levels as well as at the roof top, whereas a roof-top lumped mass was assumed for the other configurations. For this reason, larger shear forces were applied during the dynamic analyses for such cases (see Magliulo et al. 2018 for detailed descriptions).

Though some discrepancies with the original structural models arose from the limitations of the ESDoF models by its nature, it can be considered that the calibrated ESDoF systems under the above assumptions provided generally comparable estimates of structural responses of the original 3D models.

4. Fragility of Structures Designed for High-hazard

This section presents the seismic fragility functions of the code-conforming buildings for the most hazardous site, i.e. AQ, using the structural EDP responses obtained from MSA of the ESDoF systems. The derived fragility curves were also compared with those from the original 3D structural models (Section 3). The issues related to the fragility derivation for the structures at the low- and mid-hazard sites are addressed separately (to follow).

4.1. Methodology

It is a common practice in the PBEE framework that a probability model represents seismic fragility. A lognormal cumulative distribution function (CDF) is typically assumed (Ibarra and Krawinkler 2005):

$$P[\text{failure}|IM = x] = \Phi \left[\frac{\ln(x) - \eta}{\beta} \right] \quad (2)$$

where $\Phi(\bullet)$ is the standard normal CDF and η and β are the fragility functions parameters. The choice of fragility-fitting approach depends on that of structural analysis (see, for example, Iervolino 2017) and this study adopted an *EDP-based approach* utilizing the structural responses given $Sa(T)$ obtained from MSA (see Section 3). In this case, a set of two fragility function parameters $\{\eta, \beta\}$ is estimated based on the maximum likelihood approach using the EDP vectors measured at multiple IMLs, $edp_i = \{edp_1, edp_2, \dots, edp_{N_{tot,IM=x_i}}\}$ where $i = \{1, 2, \dots, m\}$, which are subsequently partitioned into two: $N_{f,IM=x_i}$ failure and $(N_{tot,IM=x_i} - N_{f,IM=x_i})$ non-failure cases. The fragility parameters are given by Eq. (3) that serves to maximize the likelihood of the entire data set being observed (Baker 2015).

$$\begin{aligned} \{\hat{\eta}, \hat{\beta}\} = \arg \max_{\eta, \beta} & \left[\sum_{i=1}^m \ln \left(\frac{N_{tot, IM=x_i}}{N_{f, IM=x_i}} \right) + N_{f, IM=x_i} \ln \left\{ \Phi \left[\frac{\ln(x_i) - \eta}{\beta} \right] \right\} \right. \\ & \left. + (N_{tot, IM=x_i} - N_{f, IM=x_i}) \cdot \ln \left\{ 1 - \Phi \left[\frac{\ln(x_i) - \eta}{\beta} \right] \right\} \right] \end{aligned} \quad (3)$$

Figure 14 shows an example of the described EDP-based fragility fitting using the MSA results (i.e. AQ soil C, URM 2st C3). Identifying the number of failure cases observed in MSA at each of the 10 IMLs ($N_{f, IM=x_i}$ in the left panel), the failure probabilities computed as $N_{f, IM=x_i}$ over $N_{tot, IM=x_i}$ (denoted with the triangle scatters in the right panel) are thoroughly fitted by a lognormal CDF (denoted with the red solid line in the right) via Eq. (3).

4.2. Results

4.2.1. URM Fragility

The fragility functions for the URM buildings were estimated as a function of $Sa(0.15s)$ for all building cases. The presented fragility functions assume the worst damage case (i.e. the larger value of the D/C ratios) of the flexure- and shear-dominated hysteresis models, which mimic the structural response of the original detailed models (Figs. 13a,b). The computed fragility function parameters are summarized in Table 7, which compares the results from the ESDoF systems with those from the original 3D models. In agreement with the discussion given in the previous section, the ESDoF systems show lower values of the median spectral acceleration causing structural failure, that is $\hat{S}a(T) = e^{\hat{\eta}}$, than the original 3D models, especially for the buildings with the E-type configuration where the error ranges between 24% and 60%. The same type of error for the C type configuration is between 1% and 6%. The values of $\hat{\beta}$ are similar between the two modeling approaches ranging approximately between 0.25 and 0.50.

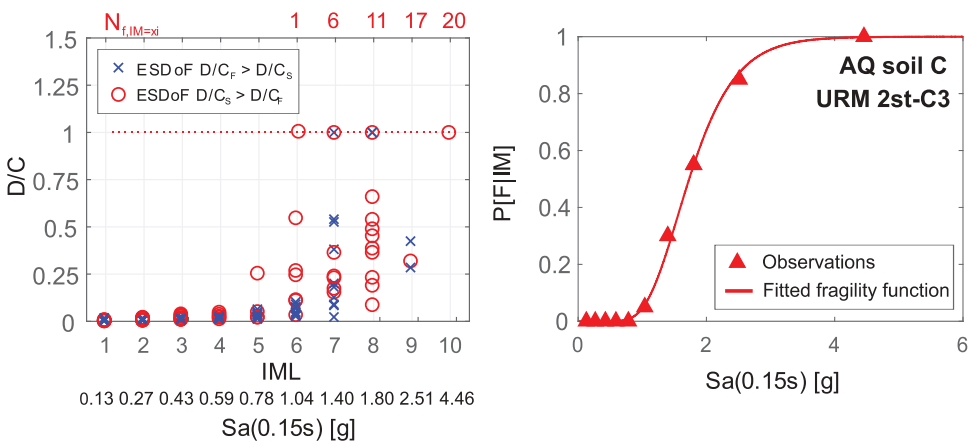


Figure 14 Example of EDP-based fragility fitting using MSA results for URM 2st C3 at AQ on soil C.

Table 7 Fragility function parameters for the URM buildings (AQ).

Model	Site Config.	AQ soil A					AQ soil C			
		C1 2st	C1 3st	E2 2st	E2 3st	E8 3st	C3 2st	E2 2st	E8 2st	E9 2st
3D model	$\hat{S}a(0.15s)[g]$	1.44	1.32	2.04	1.52	1.64	1.68	1.80	1.84	1.34
	$\hat{\beta}$	0.41	0.51	0.48	0.48	0.42	0.24	0.32	0.33	0.38
ESDoF	$\hat{S}a(0.15s)[g]$	1.52	1.31	2.55	1.88	2.26	1.73	2.44	2.32	2.14
	$\hat{\beta}$	0.40	0.44	0.50	0.51	0.52	0.33	0.34	0.37	0.30

4.2.2. RC Fragility

The fragility functions for the RC buildings were estimated as a function of spectral acceleration at the conditioning period determined for each configuration (i.e. number of stories, with or without infills). The estimated fragility function parameters and the considered IMs are provided in Table 8. It should be noted that, for some RC buildings, the failure probability given the IML corresponding to the maximum $T_R = 10^5$ years resulted to be smaller than 50% (denoted in italic) leading to the fitted parameters only governed by the failure observations at the smaller IMLs. In such cases, the fragility parameters were *re-estimated* by performing some additional analyses up to $IM = x$, $x > x_{T_R=10^5}$, at which the failure probability had exceeded $P[failure|IM = x] > 0.9$, using the same GM set for the tenth IML (denoted as 10^+ IML in the table). (Indeed, past studies on the efficient strategies for fragility function fitting (Baker 2015) recommend to run the analysis up to IMLs corresponding to probabilities of 0.7 and 0.9, for estimating median and standard deviation parameters, respectively. Herein the larger between these values was considered to re-estimate sets of fragility parameters.) Nonetheless, the results show that the fragility parameters from the ESDoFs have the maximum error of 25% in $\hat{S}a(T)$ (excluding the cases in italic) with respect to those obtained from the original models. The values of $\hat{\beta}$ vary approximately from 0.3 to 0.7.

4.2.3. Steel Fragility

Table 9 shows the fragility function parameters for the steel buildings, which were estimated as a function of $Sa(0.5s)$ and $Sa(1.0s)$ for the buildings Geo 1,2 and Geo 3,4, respectively, given the FEMA 356 criterion (ASCE, 2000) for the CBF systems. It is observed that, in most cases, the $\hat{S}a(T)$ values have a difference ranging between 2% and 26% with respect to the 3D models.

Table 8 Fragility function parameters for the RC buildings (AQ, soil C).

Model	Story Config.	3st			6st			9st		
		1.0s	0.15s	0.5s	1.5s	0.5s	0.5s	2.0s	1.0s	1.0s
		BF	IF	PF	BF	IF	PF	BF	IF	PF
3D model	$\hat{S}a(T)[g]$	4.56*	5.67*	5.84	1.72	4.47	4.57	1.14*	3.64*	3.76*
	$\hat{\beta}$	0.51*	0.52*	0.49	0.35	0.67	0.65	0.62*	0.72*	0.71*
ESDoF	$\hat{S}a(T)[g]$	3.01	4.89*	5.44	1.83	5.59	5.59	1.87*	3.81*	3.88*
	$\hat{\beta}$	0.30	0.44*	0.47	0.33	0.55	0.55	0.73*	0.61*	0.70*
ESDoF10 ⁺ IML	$\hat{S}a(T)[g]$	-	6.88	-	-	-	-	1.56	4.20	4.23
	$\hat{\beta}$	-	0.73	-	-	-	-	0.47	0.72	0.74

* $P[failure|IM_{10} = x_{T_R=10^5}] < 0.50$

Table 9 Fragility function parameters for the steel buildings (AQ).

Model	Config.	Soil A				Soil C			
		Sa(0.5s)		Sa(1.0s)		Sa(0.5s)		Sa(1.0s)	
		Geo 1	Geo2	Geo 3	Geo4	Geo 1	Geo2	Geo 3	Geo4
3D model	$\hat{S}a(T)$ [g]	3.49	5.08*	2.11	2.34*	3.67	4.47	2.56	2.04
	$\hat{\beta}$	0.42	0.10*	0.37	0.57*	0.52	0.29	0.45	0.39
ESDoF	$\hat{S}a(T)$ [g]	3.55	3.67	2.14*	2.26*	3.40	3.53	1.90**	1.92**
	$\hat{\beta}$	0.35	0.32	0.08*	0.10*	0.32	0.29	0.06**	0.06**
ESDoF 10+IML	$\hat{S}a(T)$ [g]	-	-	2.19	2.30	-	-	2.09	2.24
	$\hat{\beta}$	-	-	0.28	0.27	-	-	0.28	0.27

* $P[failure|IM_{10} = x_{T_r=10^5}] < 0.50$

** lack of responses at intermediate IMLs where $0 < P[failure|IM_i = x_i] < 1$

For Geo 3,4 on soil A, the failure probability conditional to the largest investigated IML did not exceed 50%, thus the parameters were re-estimated as described. For Geo 3,4 on soil C, the fragility resulted to be very steep because the lower IMs, at which failures are not observed, are abruptly separated from the higher IMs where failure is almost certain, according to the response sample. The parameters for such cases were re-estimated including the sample additionally obtained at the intermediate IMs using the GM set for the closet IML. In both cases, re-estimated parameters showed a similar median but larger $\hat{\beta}$ values.

Excluding such special cases, the values of $\hat{\beta}$ from the ESDoFs with the equivalent global EDPs were all around 0.30, generally smaller than the results from the 3D models using the local strain-based failure criterion.

4.2.4. PRC Fragility

The fragility functions parameters for the PRC buildings were estimated as a function of $Sa(2.0s)$ and are given in Table 10 for both the displacement-based and connection-shear-based global collapse conditions. In most cases, the collapse fragility curves associated with the two different EDPs showed similar trends due to the proximity of the EDP thresholds on the pushover curves, yet the local collapse mechanism appeared still more critical. It

Table 10 Fragility function parameters for the PRC buildings (AQ).

Model/EDP	Site Config.	Soil A				Soil C			
		Geo 1	Geo2	Geo 3	Geo4	Geo 1	Geo2	Geo 3	Geo4
3D model/Disp.	$\hat{S}a(2.0s)$ [g]	0.69**	0.76*	0.75*	0.76*	1.13*	1.07**	1.18*	1.07**
	$\hat{\beta}$	0.08**	0.09*	0.09*	0.09*	0.09*	0.08**	0.11*	0.08**
ESDoF/Disp.	$\hat{S}a(2.0s)$ [g]	0.67	0.82*	0.75*	0.76*	1.10*	1.12*	1.18*	1.12*
	$\hat{\beta}$	0.33	0.11*	0.09*	0.09*	0.08*	0.09*	0.11*	0.09*
ESDoF 10+IML/Disp.	$\hat{S}a(2.0s)$ [g]	-	0.93	0.89	0.89	1.03	1.22	1.30	1.20
	$\hat{\beta}$	-	0.26	0.29	0.29	0.22	0.17	0.18	0.19
3D model/Conn.	$\hat{S}a(2.0s)$ [g]	0.49*	0.38**	0.75*	0.76*	0.56**	0.56**	1.20*	1.09*
	$\hat{\beta}$	0.24*	0.05**	0.09*	0.09*	0.05**	0.05**	0.11*	0.08*
ESDoF/Conn.	$\hat{S}a(2.0s)$ [g]	0.67	0.74*	0.75*	0.77*	0.79	1.09*	1.12*	1.08*
	$\hat{\beta}$	0.33	0.08*	0.09*	0.09*	0.24	0.08*	0.09*	0.08*
ESDoF 10+IML/Conn.	$\hat{S}a(2.0s)$ [g]	-	0.80	0.85	0.98	-	1.06	1.18	1.09
	$\hat{\beta}$	-	0.21	0.28	0.42	-	0.23	0.15	0.19

* $P[failure|IM_{10} = x_{T_r=10^5}] < 0.50$

** lack of responses at intermediate IMLs where $0 < P[failure|IM_i = x_i] < 1$

should be noted that most of the cases required to re-estimate the parameters as the initial ones were governed by the failure observations at the smaller IMLs (see the previous section), though it didn't significantly affect the median trend. The ESDoF-based estimates of fragility parameters show good consistency with the original models except ones associated with the connection collapse for Geo 1,2 because of the difference in mass assumption. The range of $\hat{S}a(T)$ is approximately 0.70–1.20 for both the collapse conditions. With respect to $\hat{\beta}$, the re-estimated values range from 0.2 to 0.4.

4.3. Verification of Seismic Fragility Models

This section verifies the fragility models presented above, through the comparisons of the failure rates with the 3D structural models. Since seismic hazard at each site of interest was obtained only up to the intensity measure value with $T_R = 10^5$ years, that is $x_{T_R=10^5}$, the failure rates of the RINTC project were computed with Eq. (4) which gives a conservative approximation of the *true* rate in Eq. (1), assuming $P[\text{failure}|IM = x] = 1$ for IMs with an exceedance return period larger than $T_R = 10^5$ years.

$$\lambda_f = \int_0^{x_{T_R=10^5}} P[\text{failure}|IM = x] \cdot |d\lambda_x| + 10^{-5} \quad (4)$$

In a similar manner, the failure rates were evaluated also using the fragility functions estimated from the ESDoF systems via Eqs. (2–4), that is, substituting $P[\text{failure}|IM = x_i] = \Phi\left[\frac{\ln(x_i) - \hat{\eta}}{\hat{\beta}}\right]$, where $i = \{1, 2, \dots, 10\}$, into Eq. (4). Then, they are compared in Fig. 15 with those computed from the original 3D structural models (using the re-estimated parameters where applicable). The results show that, in general, the failure rates computed using the ESDoF models are of the same order of magnitude as those from 3D models' fragilities.

5. Fragility for Low- and Mid-hazard Sites

The issue concerning the structures designed for low-to-mid seismicity sites is that there is a lack of failure cases from dynamic analyses. In fact, it was not possible to obtain fragility curves for the MI and NA sites from the structural response at the investigated IMLs neither from the 3D structural models nor the ESDoF systems. Hence, this section investigates the fragility functions of the structures by performing MSA at additional IMLs utilizing the ESDoF systems. The following first introduces the issues on GM record selection for the additional IMLs, followed by the resulting fragility curves and failure rates.

5.1. Issues on Ground Motion Record Selection

Considering that no or quite few failure cases had been observed up to the largest IML corresponding to $T_R = 10^5$ years, it is expected to perform MSA at additional – much larger in fact – GM intensity levels for deriving fragility functions of the structures designed for the low-to-mid seismicity sites. In order to deepen the effects of selection and scaling of GM records on the resulting seismic fragility and risk, two strategies for GM selection were pursued. The first strategy was (1) to scale the hazard-consistent (CS-based) record sets

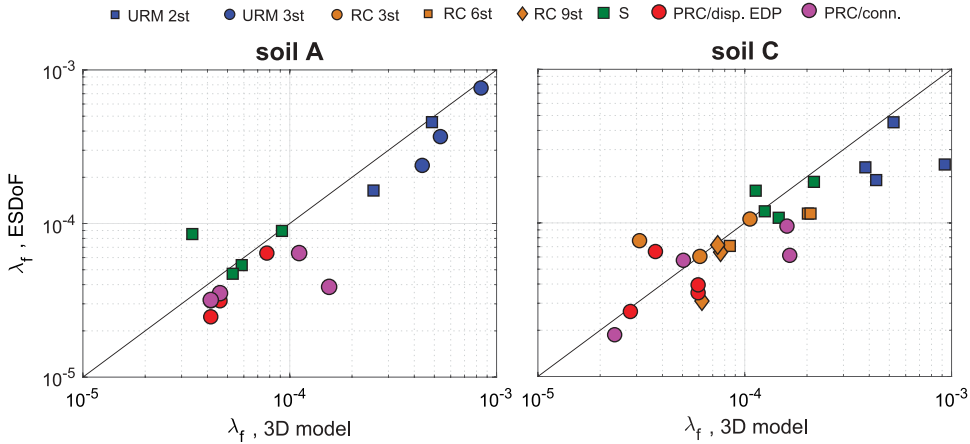


Figure 15 Verification of the ESDoF-based fragility models (AQ).

corresponding to $T_R = 10^5$ up to larger IMLs, without any reselection of GM records for the site at hand. The results from this strategy are hereafter referred to as CS-scaled. The second strategy was (2) to use a unique set of 20 GM records representing large seismic events (moment magnitude within 6.5–6.9, recorded on firm soil (Vamvatsikos and Cornell 2006)³ for any further IMLs.

The major reason for utilizing this record set (denoted as PEER, after the database), even despite the different rupture features from those expected, is the comparability with many studies and applications in the literature, in the context of collapse fragility assessment via *incremental dynamic analysis* (IDA). Regardless of the GM selection, the analyses were performed until observing failure in more than 90% of the records at the last analyzed IML.

In Fig. 16a,b the mean GM response spectra of these two cases are compared at the two arbitrarily selected IMLs of $Sa(0.5s)$ corresponding to $T_R = 7.4 \times 10^4$ and $T_R = 4.4 \times 10^7$ years for the site NA soil C, as well as with the corresponding conditional mean spectrum (CMS) from PSHA, which should be the target for the record selection. For both the return periods, the mean spectrum (of the maximum horizontal component) of the PEER GM features larger spectral ordinates than the CS-scaled GM set and the target CMS.⁴ Correspondingly, MSA had to be carried out, in the cases of using the CS-scaled records for some RC structures, up to an IM with 10^8 years for observing failure in more than 90% of records. These differences are expected to be reflected on the estimates of fragility parameters; therefore, the fragility functions estimated using Eqs. (2 and 3) under the two different GM scenarios will be discussed.

5.2. Results

The following presents the fragility functions for the low-to-mid hazard sites, each of which is expressed in terms of the same IM as that used for the corresponding structural type and configuration of the AQ buildings.

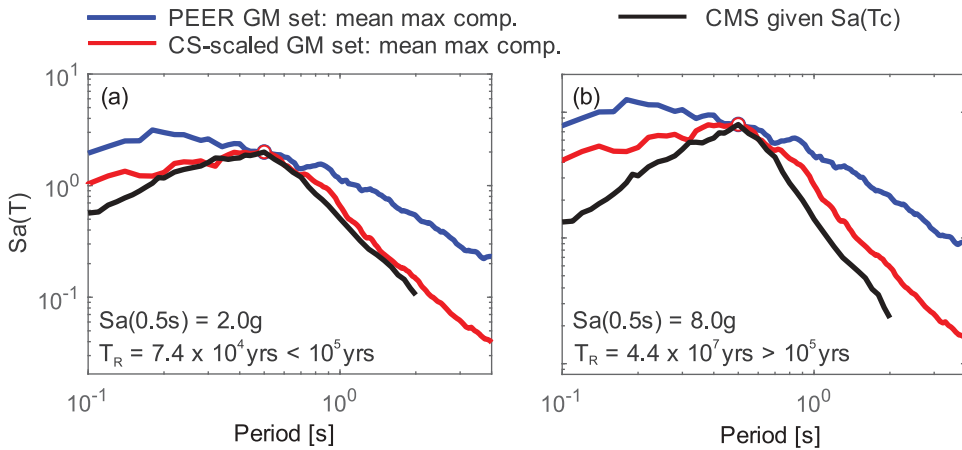


Figure 16 Comparisons of the GM response spectra for the mid-hazard site (NA, soil C).

5.2.1. URM Fragility

Tables 11 and 12 provide the fragility functions of the URM buildings located at NA and MI sites. As expected from the spectral shapes shown in Fig. 16, the PEER GM set provided the lower estimates of $\hat{S}a(T)$ than the CS-scaled one for both of the sites (even by 54%). The $\hat{\beta}$ parameter also becomes larger when estimated using the CS-scaled GM set, ranging between 0.40 and 0.70 under the CS-scaled set and between 0.30 and 0.50 under the PEER GM set.

5.2.2. RC Fragility

It is for the RC buildings that the choice of GM records affects most significantly the estimated fragility function parameters (Table 13). Especially for some short period structures (e.g. 3st PF, 6st IF/PF), $\hat{S}a(T)$ from the CS-scaled GM set is more than 60% larger than the corresponding value from the PEER GM set. It is considered that, for the RC frames with the masonry infills, the lateral stiffness changes as damage in the masonry infills progresses, thus the collapse fragility could possibly be more sensitive to the spectral ordinates in the range of vibration periods longer than T^* , as argued by specific literature; e.g. (O’Reilly and Sullivan 2018). The same trend is observed in this group for $\hat{\beta}$.

Table 11 Fragility function parameters for the URM buildings (NA).

GM type	Site	NA soil A			NA soil C					
	Config.	C3 2st	C4 3st	E8 2st	C1 2st	C4 2st	C3 3st	C5 3st	E2 3st	E8 3st
CS-scaled	$\hat{S}a(0.15s)[g]$	2.53	1.96	3.96	2.44	2.69	2.01	2.10	4.29	4.91
	$\hat{\beta}$	0.50	0.51	0.62	0.47	0.46	0.40	0.43	0.69	0.61
PEER	$\hat{S}a(0.15s)[g]$	1.91	1.53	2.61	1.68	1.88	1.48	1.53	2.12	2.27
	$\hat{\beta}$	0.35	0.34	0.46	0.37	0.34	0.34	0.33	0.44	0.47

Table 12 Fragility function parameters for the URM buildings (MI).

GM type	Site Config.	MI soil A						MI soil C						
		C3 2st	C4 2st	C2 3st	C6 3st	E2 2st	E2 3st	C1 2st	C7 2st	C2 3st	E2 2st	E2 3st	E8 3st	E9 3st
CS-scaled	$\hat{S}a(0.15s)[g]$	2.04	2.30	1.86	1.92	4.28	3.64	2.41	2.60	2.14	4.78	4.08	4.35	1.95
	$\hat{\beta}$	0.40	0.36	0.42	0.36	0.56	0.62	0.44	0.39	0.49	0.61	0.59	0.68	0.40
PEER	$\hat{S}a(0.15s)[g]$	1.68	1.88	1.57	1.58	2.63	2.12	1.68	1.89	1.57	2.62	2.12	2.27	1.67
	$\hat{\beta}$	0.37	0.34	0.38	0.36	0.44	0.44	0.37	0.35	0.38	0.44	0.44	0.47	0.30

Table 13 Fragility function parameters for the RC buildings (NA and MI, soil C).

Site/GM type	T	3st			6st			9st		
		1.0s	0.15s	0.5s	1.5s	0.5s	0.5s	2.0s	1.0s	1.0s
		BF	IF	PF	BF	IF	PF	BF	IF	PF
NA/CS-scaled	$\hat{S}a(T)[g]$	2.66	11.7	5.64	2.08	9.75	10.7	1.14	2.42	2.23
	$\hat{\beta}$	0.22	0.84	0.50	0.31	0.54	0.55	0.24	0.25	0.25
NA/PEER	$\hat{S}a(T)[g]$	1.58	3.17	2.78	1.41	3.94	4.09	0.97	1.30	1.30
	$\hat{\beta}$	0.39	0.46	0.37	0.36	0.41	0.49	0.06	0.45	0.53
MI/CS-scaled	$\hat{S}a(T)[g]$	2.72	5.08	4.93	2.21	5.58	6.47	1.78	5.09	4.38
	$\hat{\beta}$	0.44	0.55	0.69	0.33	0.69	0.65	0.35	0.40	0.37
MI/PEER	$\hat{S}a(T)[g]$	1.30	2.39	1.93	1.00	1.89	1.88	0.85	1.81	1.41
	$\hat{\beta}$	0.40	0.48	0.35	0.33	0.34	0.44	0.29	0.54	0.60

5.2.3. Steel Fragility

The same trends are observed also for the steel buildings. As summarized in Table 14, the difference in $\hat{S}a(T)$ between the two GM sets varies approximately between 20% and 40%. The $\hat{\beta}$ parameter ranges between 0.2 and 0.4. It is particular for this structural type that the fragility parameters from the PEER GM set are similar across the sites, which arises from the fact that the site hazard made little difference in its seismic design as the earthquake is not the design-ruling action.

5.2.4. PRC Fragility

Table 15 summarizes the estimated fragility parameters for the PRC buildings with respect to the collapse conditions based on the two different EDPs. It should be noted that, as reported in Magliulo et al. (2018), the maximum connection shear capacities of the Geo 3

Table 14 Fragility function parameters for the steel buildings (NA and MI).

Site/GM type	IM Config.	Soil A				Soil C			
		$Sa(T = 0.5s)$		$Sa(T = 1.0s)$		$Sa(T = 0.5s)$		$Sa(T = 1.0s)$	
		Geo 1	Geo2	Geo 3	Geo4	Geo 1	Geo2	Geo 3	Geo4
NA/CS-scaled	$\hat{S}a(T)[g]$	4.10	4.13	2.20	2.39	4.00	4.09	2.51	2.74
	$\hat{\beta}$	0.45	0.40	0.22	0.24	0.39	0.36	0.34	0.35
NA/PEER	$\hat{S}a(T)[g]$	3.02	3.16	1.82	1.91	3.02	3.16	1.82	1.91
	$\hat{\beta}$	0.27	0.25	0.38	0.30	0.27	0.25	0.38	0.30
MI/CS-scaled	$\hat{S}a(T)[g]$	4.49	4.59	2.36	2.49	4.51	4.58	2.95	3.08
	$\hat{\beta}$	0.37	0.36	0.24	0.25	0.36	0.35	0.39	0.31
MI/PEER	$\hat{S}a(T)[g]$	3.02	3.16	1.82	1.90	3.02	3.16	1.82	1.90
	$\hat{\beta}$	0.27	0.25	0.38	0.30	0.27	0.25	0.38	0.30

Table 15 Fragility function parameters for the PRC buildings (NA and MI).

Site/EDP/GM type	Config.	Soil A				Soil C			
		Geo 1	Geo2	Geo 3	Geo4	Geo 1	Geo2	Geo 3	Geo4
NA/Disp./CS-scaled	$\hat{S}a(2.0s)[g]$	0.79	0.93	1.09	1.09	1.06	1.28	1.35	1.35
	$\hat{\beta}$	0.29	0.29	0.31	0.31	0.23	0.15	0.25	0.25
NA/Disp./PEER	$\hat{S}a(2.0s)[g]$	0.65	0.83	1.00	1.00	0.78	1.07	1.00	1.01
	$\hat{\beta}$	0.27	0.22	0.20	0.24	0.20	0.14	0.20	0.21
MI/Disp./CS-scaled	$\hat{S}a(2.0s)[g]$	0.99	0.77	1.26	1.30	1.09	1.22	1.47	1.52
	$\hat{\beta}$	0.30	0.26	0.28	0.26	0.35	0.23	0.27	0.27
MI/Disp./PEER	$\hat{S}a(2.0s)[g]$	0.63	0.68	0.86	0.88	0.63	0.77	0.89	0.88
	$\hat{\beta}$	0.21	0.23	0.27	0.26	0.21	0.26	0.28	0.26
NA/Conn./CS-scaled	$\hat{S}a(2.0s)[g]$	0.80	0.93	0.20	1.16	1.06	1.17	1.25	1.34
	$\hat{\beta}$	0.29	0.29	0.14	0.37	0.23	0.21	0.25	0.22
NA/Conn./PEER	$\hat{S}a(2.0s)[g]$	0.67	0.83	0.23	1.13	0.81	1.03	0.99	1.06
	$\hat{\beta}$	0.25	0.22	0.11	0.30	0.22	0.13	0.21	0.22
MI/Conn./CS-scaled	$\hat{S}a(2.0s)[g]$	0.90	0.75	0.14	0.14	0.99	1.08	0.19	0.20
	$\hat{\beta}$	0.25	0.27	0.04	0.04	0.30	0.25	0.02	0.14
MI/Conn./PEER	$\hat{S}a(2.0s)[g]$	0.57	0.64	0.20	0.14	0.57	0.73	0.20	0.21
	$\hat{\beta}$	0.24	0.18	0.14	0.04	0.24	0.23	0.14	0.12

and/or 4 buildings for the sites NA and MI are attained within the elastic branch of the pushover curve due to the low design demand for the sites, thus resulting in $\hat{S}a(T) < 0.20g$. Compared to the other structural types, the choice of the GM sets did not apparently affect the resulting fragility parameters presumably because of the GM scaling at a relatively longer conditioning period.

5.3. Comparisons of Failure Rates

The failure rates of the considered buildings for the sites NA and MI were also computed using Eq. (4) in the same manner, as done for the AQ buildings. Figure 17 presents the

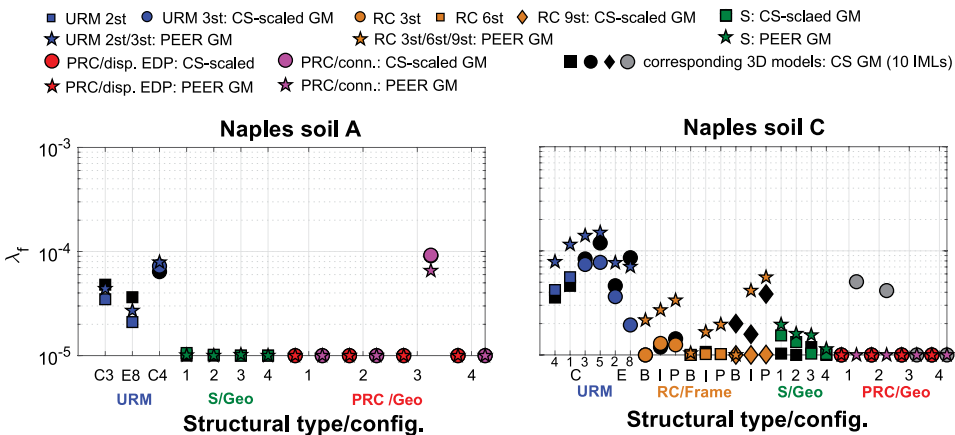


Figure 17 Comparisons of failure rates for the mid-hazard site (NA) computed with fragilities from the two different record sets.

computed rates for the NA site with different colors and markers corresponding to different structural typologies and configurations, models, GM record sets, and collapse conditions.

Although the estimated fragility parameters showed substantial dependency on the used GM records set, it can be observed that the resulting failure rates, thanks to the filtering effect of low exceedance rates of the largest IM values, are relatively similar. Note that the markers aligned on the 10^{-5} rate mean that, regardless the used GM set, only an upper bound to the failure rate could be provided because the integral part of Eq. (4) was negligible.

5.4. Comparison across Sites and Structural Types

The estimated fragility functions of the prototype buildings were compared between the three cities with different levels of seismicity. Figure 18 shows the logarithmic mean and plus/minus one standard deviation of $S_a(T)$, normalized by the design spectral acceleration at the conditioning period of the corresponding structure, $S_{aSLV}(T)$. The abscissa is in ascending order of the design hazard. It is clearly observed that the $\hat{S}_a(T)/S_{aSLV}(T)$ ratio tends to decrease with the increasing hazard at the site due to the comparable median capacities and site-dependent design seismic actions; when compared among the results from the CS-scaled and CS-based GM sets, the $\hat{S}_a(T)/S_{aSLV}(T)$ ratios of the same structural type for AQ are smaller than those for MI, approximately by a factor of 3–9 in most cases, accordingly to the differences in the design seismic actions (see Fig. 1b). The observation herein is consistent with the trend of the failure rates of the structures analyzed in the RINTC project (RINTC-Workgroup 2018), as well as with that of the strength reduction factor discussed in Suzuki, Baltzopoulos, and Iervolino (2018). As far as the prototype buildings examined under particular design and modeling assumptions are concerned, the URM buildings turned out to be the most vulnerable, followed by the steel/PRC and RC buildings, which is also consistent to the project’s findings (Iervolino, Spillatura, and Bazzurro 2018).

6. Conclusions

This study developed global-collapse seismic fragility functions of the Italian NTC code-conforming buildings of the RINTC project through pushover-based SDoF approximation. For the purposes of this investigation, some regular buildings, belonging to four different

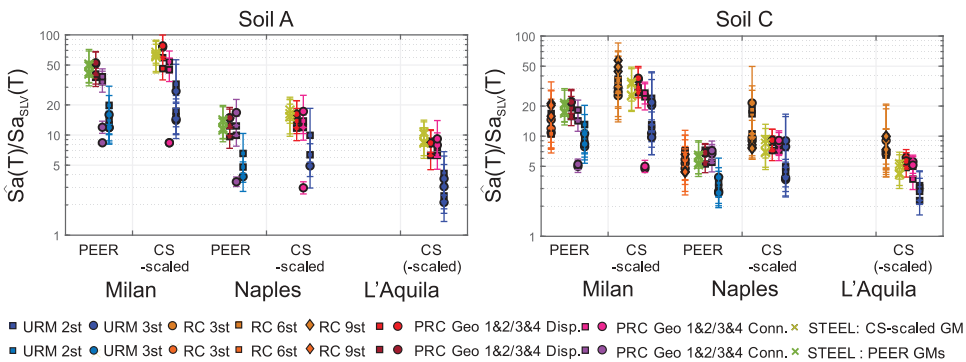


Figure 18 Estimated collapse margin ratios for all considered buildings.

structural types and located at three Italian locations, were selected. The fragility functions, expressed in terms of spectral acceleration at a period close to the fundamental vibration periods of the corresponding structure, were constructed through an EDP-based approach in conjunction with maximum likelihood estimation fitting method. For all considered cases, the ESDoF systems and the computed fragility functions were validated through the comparison with the 3D models, in terms of dynamic structural response (i.e. demand-capacity ratio of the engineering demand parameter of interest) and annual collapse rate.

The study mainly provided hazard-consistent fragility curves for the buildings designed at the high-hazard site (L'Aquila), which were verified through the comparison in terms of failure rate; i.e. the main results of the RINTC project. For the sites exposed to low-to-mid design hazard (Milan and Naples), structural analysis at IM levels with very large return periods of exceedance was needed to fit the fragility functions (i.e. to observe a sufficient number of failures). In such cases, the possible approaches for fragility derivation were explored using two alternative GM sets, addressing the issues in the GM record selection (i.e. hazard-consistency and GM scaling to accelerations corresponding to large return periods of exceedance).

The findings also allowed to observe that the ratio of the median spectral acceleration causing structural failure, to the horizontal elastic spectral acceleration with the return period used for design, tends to decrease with the increasing design hazard.

These results from the extensive examination on seismic fragility and risk across multiple locations, particularly in the Italian context, could contribute to the development of risk-based seismic design of structures in future building codes.

Notes

1. In general, the choice of analysis methods for structural design of masonry buildings is made depending on the regularity of the structure and the hazard level at the site.
2. Applying the same damping ratio (5%) for the three different structural types/configurations (RC, steel, and PRC) could be discussed; however, this study rather prioritized the agreement between the ESDoF systems and the corresponding 3D structural models avoiding the discrepancies due to arbitrary adjustments of the damping ratios. For the details of the typology-specific modeling, see the cited papers.
3. In fact, 20 two-horizontal-component accelerometric waveforms were selected from the record set used in the cited paper, which contains the 30 single-component GM records.
4. At these IM levels, the scaling factors were quite large; this is inevitable due to the acceleration values to observe a significant number of failures in the buildings designed at the low-to-mid hazard sites. In fact, the average of the scaling factors at the IM level corresponding to $T_R = 4.4 \times 10^7$ years was 17 for the CS-based record set and 26 for the PEER GM set. The effects of scaling on structural response are discussed in literature; see for example Luco and Bazzurro (2007), where similar ranges of scaling factors are investigated. However, note that very large accelerations may have a limited impact on the failure rate because of their small exceedance rates (i.e. Eq. (1)).

Acknowledgments

The study presented in this article was developed within the activities of the ReLUIIS-DPC 2014–2018 research program, funded by *Presidenza del Consiglio dei Ministri – Dipartimento della Protezione Civile*; however, opinions and conclusions do not necessarily reflect those of the funding entity. Data and technical supports from the RINTC workgroup are gratefully acknowledged. The authors are also thankful to the two anonymous reviewers who helped to greatly improve the quality of the paper.

ORCID

Akiko Suzuki  <http://orcid.org/0000-0001-9523-3488>

Iunio Iervolino  <http://orcid.org/0000-0002-4076-2718>

References

- Altoontash, A. 2004. Simulation and damage models for performance assessment of reinforced concrete beam-column joints. Ph.D. thesis, Department of Civil and Environmental Engineering, Stanford University [Advisor: G. Deierlein].
- ASCE. 2000. Prestandard and commentary for the seismic rehabilitation of buildings, Report FEMA-356, Washington, DC, USA.
- ASCE. 2017. Minimum design loads for buildings and other structures, ASCE/SEI 7-16, American Society of Civil Engineers, Reston, VA, USA.
- Baker, J. W. 2015. Efficient analytical fragility function fitting using dynamic structural analysis. *Earthquake Spectra* 31 (1): 570–99. doi:10.1193/021113EQS025M.
- Baltzopoulos, G., R. Baraschino, I. Iervolino, and D. Vamvatsikos. 2017. SPO2FRAG: Software for seismic fragility assessment based on static pushover. *Bulletin of Earthquake Engineering* 15 (10): 4399–425. doi:10.1007/s10518-017-0145-3.
- Cattari, S., D. Camilletti, S. Lagomarsino, S. Bracchi, M. Rota, and A. Penna. 2018. Masonry Italian code-conforming buildings. part 2: Nonlinear modelling and time-history analysis. *Journal of Earthquake Engineering* 22 (sup2): 2010–40. doi:10.1080/13632469.2018.1541030.
- CEN. 2004. Eurocode 8: design provisions for earthquake resistance of structures, part 1.1: General rules, seismic actions and rules for buildings, EN1998-1.
- Christopoulos, C., R. Tremblay, H. J. Kim, and M. Lacerte. 2008. Self-centering energy dissipative bracing system for the seismic resistance of structures: Development and validation. *Journal of Structural Engineering* 134 (1): 96–107. doi:10.1061/(ASCE)0733-9445(2008)134:1(96).
- CNR 10025/98. 2000. Istruzioni per il progetto, l'esecuzione ed il controllo delle strutture prefabbricate in calcestruzzo (in Italian).
- Cornell, A. C. 1968. Engineering seismic risk analysis. *Bulletin of the Seismological Society of America* 58 (5): 1583–606.
- Cornell, A. C., and H. Krawinkler. 2000. Progress and challenges in seismic performance assessment. *Pacific Earthquake Engineering Research Center News* 3:1–3. CA, USA.
- CS.LL.PP. 2008. Norme tecniche per le costruzioni (in Italian).
- CS.LL.PP. 2018. Aggiornamento delle norme tecniche per le costruzioni (In Italian).
- D'ayala, D. F., D. Vamvatsikos, and K. Porter. 2014. GEM guidelines for analytical vulnerability assessment of low/mid-rise buildings, vulnerability global component project. doi:10.13117/GEM.VULN-MOD.TR2014.12.
- De Luca, F., D. Vamvatsikos, and I. Iervolino. 2013. Near-optimal piecewise linear fits of static pushover capacity curves for equivalent SDOF analysis. *Earthquake Engineering & Structural Dynamics* 42 (4): 523–43. doi:10.1002/eqe.2225.
- Fajfar, P. 2000. A nonlinear analysis method for performance-based seismic design. *Earthquake Spectra* 16 (3): 573–92. doi:10.1193/1.1586128.
- FEMA. 2013. *Recommended seismic design criteria for new steel moment-frame buildings: FEMA 350*. Washington, DC, USA: FEMA.
- Franchin, P., L. Ragni, M. Rota, and A. Zona. 2018. Modelling uncertainties of Italian code-conforming structures for the purpose of seismic response analysis. *Journal of Earthquake Engineering* 22 (sup2): 1964–89. doi:10.1080/13632469.2018.1527262.
- HAZUS-MH. 2003. Multi-hazard loss estimation methodology: Earthquake model – Technical manual. Accessed November 2018. <https://www.fema.gov/hazus>
- Hsiao, P., D. E. Lehman, and C. W. Roeder. 2013. Evaluation of the response modification coefficient and collapse potential of special concentrically braced frames. *Earthquake Engineering & Structural Dynamics* 42 (10): 1547–64. doi:10.1002/eqe.2286.

- Ibarra, L. F., and H. Krawinkler. 2005. *Global collapse of frame structures under seismic excitations*. CA, USA: John A. Blume Earthquake Engineering Center, Stanford University.
- Ibarra, L. F., R. A. Medina, and H. Krawinkler. 2005. Hysteretic models that incorporate strength and stiffness deterioration. *Earthquake Engineering & Structural Dynamics* 34 (12): 1489–511. doi:10.1002/eqe.495.
- Iervolino, I. 2017. Assessing uncertainty in estimation of seismic response for PBEE. *Earthquake Engineering & Structural Dynamics* 46 (10): 1711–23. doi:10.1002/eqe.2883.
- Iervolino, I., A. Spillatura, and P. Bazzurro. 2018. Seismic reliability of code-conforming Italian buildings. *Journal of Earthquake Engineering* 22 (sup2): 5–27. doi:10.1080/13632469.2018.1540372.
- Jalayer, F., and A. C. Cornell. 2003. A technical framework for probability-based demand and capacity factor design (DCFD) seismic formats, PEER Report 2003/08, CA, USA.
- Jalayer, F., H. Ebrahimian, A. Miano, G. Manfredi, and H. Sezen. 2017. Analytical fragility assessment using unscaled ground motion records. *Earthquake Engineering & Structural Dynamics* 46 (15): 2639–63. doi:10.1002/eqe.2922.
- Kohrangi, M., D. Vamvatsikos, and P. Bazzurro. 2017. Site dependence and record selection schemes for building fragility and regional loss assessment. *Earthquake Engineering & Structural Dynamics* 46 (10): 1625–43. doi:10.1002/eqe.2873.
- Kosič, M., P. Fajfar, and M. Dolšek. 2014. Approximate seismic risk assessment of building structures with explicit consideration of uncertainties. *Earthquake Engineering & Structural Dynamics* 43 (10): 1483–502. doi:10.1002/eqe.2407.
- Lagomarsino, S., A. Penna, A. Galasco, and S. Cattari. 2013. TREMURI program: An equivalent frame model for the nonlinear seismic analysis of masonry buildings. *Engineering Structures* 56:1787–99. doi:10.1016/j.engstruct.2013.08.002.
- Lin, T., C. B. Haselton, and J. W. Baker. 2013. Conditional spectrum-based ground motion selection. Part I: Hazard consistency for risk-based assessments. *Earthquake Engineering & Structural Dynamics* 42 (12): 1847–65. doi:10.1002/eqe.2301.
- Luco, N., and P. Bazzurro. 2007. Does amplitude scaling of ground motion records result in biased nonlinear structural drift responses? *Earthquake Engineering & Structural Dynamics* 36 (13): 1813–35. doi:10.1002/eqe.695.
- Magliulo, G., D. Bellotti, M. Cimmino, and R. Nascimbene. 2018. Modeling and seismic response analysis of RC precast Italian code-conforming buildings. *Journal of Earthquake Engineering* 22 (sup2): 140–67. doi:10.1080/13632469.2018.1531093.
- Manzini, C. F., G. Magenes, A. Penna, F. Da Porto, D. Camilletti, S. Cattari, and S. Lagomarsino. 2018. Masonry Italian code-conforming buildings. Part 1: Case studies and design methods. *Journal of Earthquake Engineering* 22 (sup2): 54–73. doi:10.1080/13632469.2018.1532358.
- McKenna, F., G. L. Fenves, M. H. Scott, and B. Jeremic. 2000. *Open system for earthquake engineering simulation (OpenSees)*. Berkeley, CA, USA: Pacific Earthquake Engineering Research Center, University of California. Accessed November 2018. <http://opensees.berkeley.edu/>
- O'Reilly, G. J., and T. J. Sullivan. 2018. Quantification of modelling uncertainty in existing Italian RC frames. *Earthquake Engineering & Structural Dynamics* 47 (4): 1054–74. doi:10.1002/eqe.3005.
- Pitilakis, K., H. Crowley, and A. M. Kaynia. 2014. *SYNER-G: Typology definition and fragility functions for physical elements at seismic risk*. Vol. 27. Dordrecht, Netherlands: Springer. doi:10.1007/978-94-007-7872-6.
- Ricci, P., V. Manfredi, F. Noto, M. Terrenzi, C. Petrone, F. Celano, M.T. De Risi, G. Camata, P. Franchin, G. Magliulo, et al. 2018. Modeling and seismic response analysis of Italian code-conforming reinforced concrete buildings. *Journal of Earthquake Engineering* 22 (sup2): 105–39. doi:10.1080/13632469.2018.1527733.
- RINTC-Workgroup. 2018. Results of the 2015–2017 implicit seismic risk of code-conforming structures in Italy (RINTC) project. ReLUI Report, Rete Dei Laboratori Universitari Di Ingegneria Sismica (ReLUI), Naples, Italy.
- Rota, M., A. Penna, and G. Magenes. 2010. A methodology for deriving analytical fragility curves for masonry buildings based on stochastic nonlinear analyses. *Engineering Structures* 32 (5): 1312–23. doi:10.1016/j.engstruct.2010.01.009.

- Scozzese, F., G. Terracciano, A. Zona, C. G. Della, A. Dall'Asta, and R. Landolfo. 2018. Modeling and seismic response analysis of Italian code-conforming single-storey steel buildings. *Journal of Earthquake Engineering* 22 (sup2): 2104–33. doi:[10.1080/13632469.2018.1528913](https://doi.org/10.1080/13632469.2018.1528913).
- Shome, N., and A. C. Cornell. 2000. Structural seismic demand analysis: Consideration of 'collapse'. In *Proc. 8th ASCE Spec. Conf. Probabilistic mech. Struct. Reliab.* South Bend, IN: American Society of Civil Engineers (ASCE).
- Silva, V., S. Akkar, J. Baker, P. Bazzurro, J. M. Castro, H. Crowley, M. Dolsek, C. Galasso, S. Lagomarsino, R. Monteiro, et al. 2019. Current challenges and future trends in analytical fragility and vulnerability modelling. *Earthquake Spectra* in press. doi:[10.1193/042418EQS101O](https://doi.org/10.1193/042418EQS101O).
- Suzuki, A., G. Baltzopoulos, and I. Iervolino; RINTC-Workgroup. 2018. A look at the seismic risk of Italian code-conforming RC buildings. In *Proc. 16th Eur. Conf. Earthq. Eng.*, 18–21. Thessaloniki, Greece.
- Suzuki, A. 2019. Seismic fragility assessment of code-conforming buildings in Italy, Ph.D. thesis, Dipartimento di Strutture per l'Ingegneria e l'Architettura, Università degli Studi di Napoli Federico II. [Advisor: I. Iervolino].
- Tremblay, R., M. Lacerte, and C. Christopoulos. 2008. Seismic response of multistory buildings with self-centering energy dissipative steel braces. *Journal of Structural Engineering* 134 (1): 108–20. doi:[10.1061/ASCE0733-94452008134:1108](https://doi.org/10.1061/ASCE0733-94452008134:1108).
- Vamvatsikos, D., and A. C. Cornell. 2006. Direct estimation of the seismic demand and capacity of oscillators with multi-linear static pushovers through IDA. *Journal of Earthquake Engineering and Structural Dynamics* 35 (9): 1097–117. doi:[10.1002/eqe.573](https://doi.org/10.1002/eqe.573).